Thesis for the degree
Master of Science

Submitted to the Scientific Council of the
Weizmann Institute of Science
Rehovot, Israel

עבודת גמר (תזה) לתואר
מוסמך למדעים

מוגשת למועצה המדעית של
מכון ויצמן למדע
רחובות, ישראל

By
Jonatan Piasetzky

מאת
יונתן פיסצקי

לכידה וקירור יוני איטרביום לקראת שעון אטומי אופטי
Trapping and cooling of Ytterbium ions towards optical atomic clock

Advisor: Prof. Roee Ozeri

מנחה: פרופ' רועי עוזרי

April 2019

ניסן ה'תשע"ט

1 Abstract

Trapped ions provide a very simple, yet highly controllable and reproducible quantum system, with very long coherence time and many to many interactions easily achievable. They have been used in many fields of physics and technology, and also offer great promise for the future, in the search for new physics and in applications such as precision measurements, quantum information processing and more.
In this thesis, I describe the implementation of trapping a single Yb^+ ion, and the experiments used to characterize and understand the system. I first discuss the design and construction of the apparatus, which was a major part of this work, and then the spectroscopy measurements taken and its analysis. The ion is trapped in a linear Paul trap, using RF electrodynamic fields, it is manipulated mostly with lasers in the UV and IR, and measured optically with an EMCCD camera. This thesis includes the designing of the trap, and the electronics needed for it. Then, it goes over the design and implementation of the optics and electronics needed for producing and stabilizing the required laser sources. It also covers, more briefly, the other aspects needed, which include the vacuum system design, the imaging system (detection optics) and lastly the production of the ions themselves.

2 Acknowledgments

I would like to acknowledge some of the people, responsible for making this thesis possible.
First, my advisor, Roee, for inviting and accepting me into the fascinating world of ion-trapping, showing how interesting it could be, giving me the right motivation at the right time, and off course consulting and advising regarding results, physics and future plans.
Nitzan, our group staff scientist, with a probably infinite amount of experience and knowledge, was able to help in almost any problem encountered during this work, and was the usual first (and last) stop. Next I would like to thank all of our group members: Lee, Meirav, Ruti, Tom, Ravid, Yotam, Lior and Meir for a vast amount of discussions and advisements, be it on deep underlying physical understanding, practical and technical tips, or even one of many other unrelated themes - thanks for being there for me and making my work environment pleasant and welcoming.
Lastly, the technical and administrative teams of the department, having great influence on the ability to put thought into action and create the necessary tools for the job: Guy and Gershon from the workshop, Rostyslav and Yuri from the electronics team, Yossi from IT and Perla, Rachel and Malka from the administrative side.
Outside the faculty and the professional work, I would very much like to appreciate my wife, Rotem, for the truly infinite support and understanding. She was there for me in every step of the way, enjoying my successes (was delighted to hear I finally trapped an ion!), but also being very supportive and containing through the rougher times (and there were). Other than her, off course, a big thank you goes to my parents and my family, supporting my decisions, and giving advise all through the process, and specifically my father, for drawing me into the world of experimental physics.

Contents

3 Introduction

In the last 40 years or so, experiments with trapped ions have provided contributions to many fields in physics with applications in quantum information processing, precision measurements (metrology), geodesy, communications and more. Largely this is attributed to the trapped ions tight spatial localization, isolation from external perturbations and relative ease of coherent control of internal and external degrees of freedom with high fidelity.
The need for more accurate and precise frequency standards and clocks has continued unbated for centuries, and the contributions of accurate time and frequency measurements to all sorts of fields of technology and science can hardly be overestimated. Historically, the prime application for clocks has been in navigation [1], and today it is hard to imagine our world without the use of Global Navigation Satellite Systems (GNSS), and looking forward, navigation systems based on better clocks may have unpredicted applications (for example, measuring small strains in Earth's crust for use in earthquake prediction[1] and many more).

The first caesium atomic clock, developed in 1955 [2] demonstrated use of transitions between discrete energy levels of an isolated atomic system, and provided a much more stable and accurate reference time than any standard using celestial bodies. These systems are highly reproducible, therefore making them ideal references for frequency standards, an idea attributed to Maxwell, and captured nicely in a text written by Lord Kelvin [3]:
"The recent discoveries ... indicate to us natural standard pieces of matter such as atoms of hydrogen or sodium, ready made in infinite numbers, all absolutely alike in every physical property. The time vibration of a sodium particle corresponding to any one of its modes of vibration is known to be absolutely independent if its position in the universe, and it will probably remain the same so long as the particle itself exists."

The caesium clock uses two hyperfine split levels, which resigns in the Microwave regime of electromagnetic waves, and while it is understood for some time that there are several advantages gained from moving to higher frequency standards, technical difficulties of counting oscillations in the THz frequency regime halted the transition into optical standards. Major developments in the field of femto-second lasers, and the invention of the frequency comb were able to bridge the gap between the optical and RF regimes, allowing experimentalists to finally count oscillation frequency of optical transitions, and consequently led the begining of the field of optical atomic clocks, improving the existing microwave clocks uncertainty by several orders of magnitude.

Other than lots of practical applications benefit, atomic clocks attract scientists with the ability to very precisely control and explore a simple quantum system. Some of exciting possibilities is to unveil dynamics that were not expected, and occur from "new physics" (i.e., physics not portrayed by current Standard Model), for example, current interest exists to explore the ideas of change in time of the relative strength of the fundamental forces [4][5][6], existence of new fundamental interactions [7] and new force carriers [8].

This thesis is divided into three parts, the first part consists of the theory behind trapping, producing, cooling and manipulating ions. The second part describes the experimental setup and apparatus used in this work. and the last part shows the relevant results for characterizing the system.

4 Theoretical background

4.1 Linear Paul Trap

4.1.1 Potential definition

According to Laplace equation, stable trapping of charged particles in free space using only DC fields is not possible, as there is no local minimum. The Paul trap, named after its inventor W. Paul[9], uses oscillating electric fields to overcome this fundamental limitation. In these traps, electrodes are driven with static (DC) and oscillating (RF) voltages, and are geometrically aligned to create an approximate quadrupolar spatial electric potential $\phi(x, y, z, t)$ in the center of the trapping region:

$$\Phi(\vec{r}, t) = \frac{1}{2}\left(U_x^s x^2 + U_y^s y^2 + U_z^s z^2\right) + \frac{1}{2}\cos(\Omega t)\left(U_x^{RF} x^2 + U_y^{RF} y^2 + U_z^{RF} z^2\right) \tag{4.1}$$

The potential has to fulfill the Laplace equation $\nabla^2\Phi = 0$ at every instant of time, which leads to the following geometric restrictions:

$$U_x^s + U_y^s + U_z^s = 0 \quad ; \quad U_x^{RF} + U_y^{RF} + U_z^{RF} = 0 \tag{4.2}$$

There are a few choices of producing a three-dimensional confinement albeit the restrictions. One popular such choice is the linear Paul trap, in which RF fields are applied only in two radial direction and confining along the third axial direction is done by purely static potential, giving:

$$-(U_x^s + U_y^s) = U_z^s > 0 \quad ; \quad U_x^{RF} = -U_y^{RF} \quad ; \quad U_z^{RF} = 0 \tag{4.3}$$

This can be implemented using 2 DC voltage end-caps which statically confine the ions along the z-axis (the trap axis), and 4 RF linear electrodes, forming a time-varying quadrupolar potential, which dynamically confine in the x-y plane (see 5.1).

4.1.2 Classical equations of motion

The classical equations of motion of a charged particle with mass m and charge Q that arise from such potential can be written as 3 de-coupled Ordinary Differential Equations (ODEs):

$$\ddot{x}_i = -\frac{Q}{m}(U_i^s + U_i^{RF}\cos(\Omega t)) \tag{4.4}$$

These equations can be transformed into the standard form of the Mathieu differential equation:

$$\begin{aligned} &\frac{d^2x}{d\tau^2} + (a_i - 2q_i\cos(2\tau)) = 0 \\ \text{where:} \quad &\tau \equiv \frac{\Omega t}{2}, \quad a_i \equiv \frac{4QU_i^s}{m\Omega^2}, \quad q_i \equiv \frac{2QU_i^{RF}}{m\Omega^2} \end{aligned} \tag{4.5}$$

The general class of stable solutions to the Mathieu equation follows from the Floquet theorem[10]:

$$x_i(\tau) = A_i e^{i\beta_i\tau}\sum_{n=-\infty}^{\infty} C_{2n}^{(i)} e^{i2n\tau} + B_i e^{-i\beta_i\tau}\sum_{n=-\infty}^{\infty} C_{2n}^{(i)} e^{-i2n\tau} \tag{4.6}$$

A_i and B_i are some constants that are chosen to satisfy boundary conditions, but the characteristic exponents β_i and coefficients $C_{2n}^{(i)}$ are functions of only a_i and q_i. By inserting the general solution Eq. 4.6 into the Mathieu equation Eq. 4.5, one obtains a recursion relation[11]:

$$C_{2n+2}^{(i)} - D_{2n}C_{2n}^{(i)} + C_{2n-2}^{(i)} = 0 \tag{4.7}$$

This relations yields connections between β_i, $C_{2n}^{(i)}$ and a_i, q_i, which can be expressed as a continued fraction:

$$\beta_i = a_i - q_i \left(\frac{1}{D_0 - \frac{1}{D_2 - \frac{1}{\dots}}} + \frac{1}{D_0 - \frac{1}{D_{-2} - \frac{1}{\dots}}} \right) \tag{4.8}$$

This can be evaluated numerically for β_i and the coefficients can be extracted by truncation the continued fraction for desired precision.

4.1.3 Stability analysis

A trapped particle will be stable in a 3D system, if in all three dimensions solutions simultaneously obey[12]:

$$0 \leq \beta_i \leq 1, \quad \forall i \in \{x, y, z\} \tag{4.9}$$

Thus, one can draw the stability region for each dimension in the plane $a_i - q_i$. And the special stable region that contains all points $(a_i, \quad q_i) = (0, \quad 0)$ for all i is often called the lowest stability region, most common traps work inside this region.
In linear Paul traps, there exists a line on which the oscillating field is zero, usually denoted the $\hat{z}$ axis, or the axial direction, in this direction $q_z = 0$, and confinement is due to $a_z > 0$ (the solution in $\hat{z}$ is stable for any $a_z > 0$), and we're left with finding the stable regions for the $\hat{x} - \hat{y}$ plane. All a's and q's are coupled through Laplace equation (Eq. 4.3) in the following manner:

$$\begin{aligned} q_y &= -q_x \\ a_y &= -a_x - a_z \end{aligned} \tag{4.10}$$

Which allows us to plot the stability regions as a function of only q_x and a_x for a given a_z, such a plot is shown in fig. 1 [11][13], where stability in all dimensions is obtained in the overlapped regions.

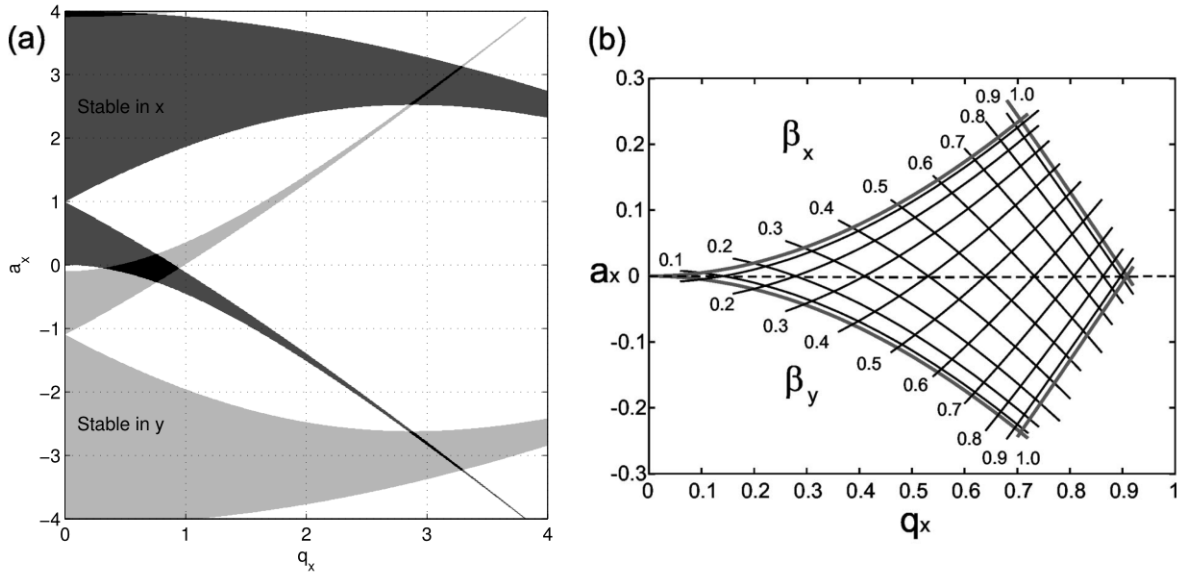

Figure 1: Stability region as a function of a_x and q_x. (a) The stability for both x and y are shown where the stable region for the entire system is seen as the overlap of both regions portrayed in black. (b) Shows a zoom in on the main (lowest) stability region

4.1.4 Ion trajectory

As mentioned, ion trap experiments are working in the lowest stability region (fig. 1 (b)), where $q^2, |a| << 1$. For which the lowest order approximation of the ion trajectory can be found by truncating at $C_{\pm 4} \approx 0$, which yields (assuming $A_i = B_i$):

$$\begin{aligned} \beta_i &\approx \sqrt{a_i + q_i^2/2} \\ x(t) &\approx A_i \cos\left(\frac{\beta_i \Omega t}{2}\right)\left[1 + \frac{q_i}{2}\cos(\Omega t)\right] \end{aligned} \tag{4.11}$$

The trajectory consists of harmonic oscillations at frequency $\omega_i = \beta_i \Omega/2 << \Omega$ (which is called the secular motion, superposed with 'intrinsic micro-motion' oscillation at the trap drive frequency Ω and with amplitude proportional to the secular motion with a $q/2$ proportionality factor. When ions are laser-cooled to sub-mK temperature, for many purposes this can be ignored, and the motion will be approximately a simple 3D harmonic oscillator motion with trap frequencies of $\omega_x, \omega_y, \omega_z << \Omega$. Figure 2 shows a plot of this type of motion.

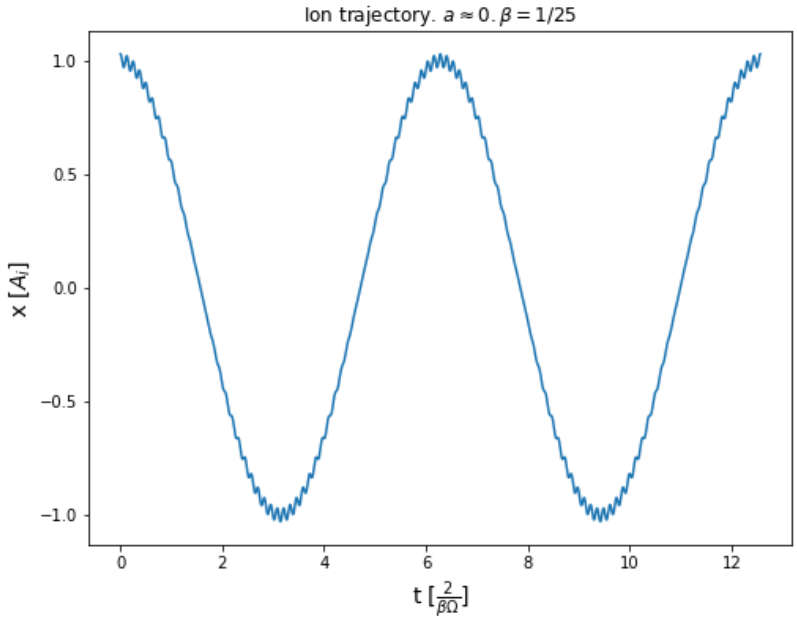

Figure 2: Ion trajectory simulation. The superimposed secular micro-motion on top of the slow harmonic oscillations is visible. The main energetic increase occurs at the positions which are furthest away from the RF null voltage

Excess micro-motion The fast oscillations of the ion at the trap drive frequency, described above, are called intrinsic micro-motion. It is an inherent effect of dynamical trapping and it is proportional to the ion harmonic amplitude, and thus gets smaller and smaller as we cool the ion.
There is another kind of micro-motion which is not proportional to the ion amplitude, and it is called excess micro-motion. It arises from stray electric at the trap center. So, for example if there exists a uniform static electric field E_s, it will add an extra term for the EOM (Eq. 4.4, which is proportional to the dot product $\vec{E} \cdot \vec{x}$, resulting in a static displacement of the ion position in each axis according to the projection of the static field on the axis, resulting in the following trajectory:

$$x(t) \approx \left(x_0^{(i)} + A_i \cos\left(\frac{\beta_i \Omega t}{2}\right)\right)\left[1 + \frac{q_i}{2}\cos(\Omega t)\right] \tag{4.12}$$

As we can see, the oscillating electric field at position x_0 results in Excess micro-motion (with amplitude $1/2\, x_0^{(i)} q_i$ which is not coupled to harmonic amplitudes (and thus does not decrease when the ion is cooled). This needs to be taken into consideration when designing a Paul trap, to allow for DC electric fields to be applied to compensate for such stray fields and reduce the excess micro-motion.

4.2 Ion-light interaction

For almost all trapped ion experimental situations it is valid and common to treat the internal degrees of freedom of the ion interacting with the laser field as a two level system (assuming the off-resonance coupling to other levels is negligible) in harmonic potential. The laser field is treated classically, which can be justified by the large number of photons used in these experiments. The total Hamiltonian of the system is:

$$\mathcal{H} = \mathcal{H}_m + \mathcal{H}_e + \mathcal{H}_i \tag{4.13}$$

where $\mathcal{H}_m$ is the motional Hamiltonian, $\mathcal{H}_e$ is the internal electronic Hamiltonian and $\mathcal{H}_I$ is the interaction of the ion with the applied light fields.
The two atomic electronic levels are separated by energy $\hbar\omega_0$ and denoted $|e\rangle$ and $|g\rangle$ for the excited and ground state respectively giving:

$$\mathcal{H}_e = \frac{\hbar\omega_0}{2}(|e\rangle\langle e| - |g\rangle\langle g|) = \frac{\hbar\omega_0}{2}\sigma_z \tag{4.14}$$

When trap parameters are chosen s.t. $a_i, q_i << 1$ in all dimensions (see 4.1), it is safe to approximate the motion of the ion as a motion of a 3-D static harmonic potential. For simplicity we'll treat this in only one dimension (say $\hat{x}$), but it is easy to generalize:

$$\mathcal{H}_m = \hbar\omega_x\left(a^\dagger a + \frac{1}{2}\right) \tag{4.15}$$

Where ω_x is the trap frequency.

For the last term, it is assumed to be sufficient to treat the interaction of the ion and the light with the leading order in the multi-pole expansion, justified by the fact that the size of the wavefunction of the ion is much smaller than the laser field's wavelength. In this work we only consider dipole allowed transitions, so we use the familiar dipole approximation. This gives the following interaction Hamiltonian:

$$\mathcal{H}_i = \frac{\hbar\Omega}{2}(|g\rangle\langle e| + |e\rangle\langle g|)\left(e^{i(k\hat{x}-\omega_l t+\phi)} + e^{-i(k\hat{x}-\omega_l t+\phi)}\right) = \frac{\hbar\Omega}{2}(\sigma_+ + \sigma_-)\left(e^{i(k\hat{x}-\omega_l t+\phi)} + e^{-i(k\hat{x}-\omega_l t+\phi)}\right)$$
$$\Omega = \frac{eE_0}{\hbar}|\langle e|\vec{r}\cdot\hat{\epsilon}|g\rangle| \tag{4.16}$$

Where Ω is the Rabi frequency given by the dipole approximation, ω_l is the laser's angular frequency and k is the laser's wavenumber.
The Hamiltonian is time dependent, and it is very convenient to move to the interaction picture with the free Hamiltonian $\mathcal{H}_0 = \mathcal{H}_m + \mathcal{H}_e$ and the interaction $\mathcal{H}_i$, and then applying the rotating-wave approximation (RWA), i.e., disregarding terms that oscillate very fast, when the laser frequency is close to the transition frequency $\delta \equiv \omega_l - \omega_0 << \omega_0$. Further, we define the Lamb-Dicke parameter $\eta = k\sqrt{\hbar/2m\omega_x}$ and under the assumptions that $\eta << 1, \quad |a_i|, q_i^2 << 1$ we get the simpler interaction Hamiltonian [11]:

$$\mathcal{H}_i(t) = \frac{\hbar\Omega_0}{2}\sigma_+ \exp\left\{i\eta\left(\hat{a}e^{-i\omega_x t} + \hat{a}^\dagger e^{i\omega_x t}\right)\right\}e^{i(\phi-\delta t)} \quad + \text{h.c} \tag{4.17}$$

Where we defined the scaled Rabi frequency as $\Omega_0 = \Omega/(1 + q_i/2)$.
We can expand the exponent in Eq. 4.17, to get detuning dependent coupling of different motional

quanta states coupled with the electronic transition (sidebands). In the Lamb-Dicke regime ($\eta^2(2n+1) << 1$, where n is the motional quanta), we expand only to the lowest order in η, thus getting only three resonances.
The first one is received for zero detuning ($\delta = 0$), and is called the carrier resonance:

$$\mathcal{H}_{car} = \frac{\hbar\Omega_0}{2}\Big(\sigma_+ e^{i\phi} + \sigma_- e^{-i\phi}\Big) \tag{4.18}$$

This Hamiltonian will give rise to transitions which retain motional quanta ($|n\rangle|g\rangle \leftrightarrow |n\rangle|e\rangle$) with Rabi frequency of Ω_0.
The two other resonances are called first red and blue sidebands:

$$\begin{aligned}\mathcal{H}_{rsb} &= \frac{\hbar\Omega_0\eta}{2}\Big(a\sigma_+ e^{i\phi} + a^\dagger\sigma_- e^{-i\phi}\Big)\\ \mathcal{H}_{bsb} &= \frac{\hbar\Omega_0\eta}{2}\Big(a^\dagger\sigma_+ e^{i\phi} + a\sigma_- e^{-i\phi}\Big)\end{aligned} \tag{4.19}$$

They occur at a detuning of $\delta = -/+\omega_x$, with Rabi frequencies of $\Omega_{n,n-1} = \Omega_0\sqrt{n}\eta$ and $\Omega_{n,n+1} = \Omega_0\sqrt{n+1}\eta$ for the red and blue sidebands respectively. The red sideband couples the states $|n\rangle|g\rangle \leftrightarrow |n-1\rangle|e\rangle$, while the blue couples $|n\rangle|g\rangle \leftrightarrow |n+1\rangle|e\rangle$.
In most dipole transitions and for typical Paul traps, the natural linewidth of the transition is larger than the trap secular frequency ($\Gamma > \omega_i$), which is called the unresolved sideband regime (in order to get to motional ground state and $1\mu K$ temperature a use of a resolved sideband cooling laser is needed, usually an quadrupole transition is used), and in this regime we can no longer disregard spontaneous emission.
Spontaneous emission arises from coupling of the excited state to the E.M vacuum (which we don't get since we treated the field classically), but one can add it manually through the Lindblad master equation which describes the time evolution of an open quantum system with Markovian and time-homogeneous dynamics [14]:

$$\begin{aligned}\frac{\partial\rho}{\partial t} &= -\frac{i}{\hbar}[H,\rho] + \mathcal{L}(\rho)\\ \mathcal{L}(\rho) &= \sum_n\left(C_n\rho C_n^\dagger - \frac{1}{2}\Big\{C_n^\dagger C_n,\rho\Big\}\right)\end{aligned} \tag{4.20}$$

The Lindblad operator describing spontaneous emission is given by:

$$C_{eg} = \sqrt{\Gamma}\,|g\rangle\langle e| \tag{4.21}$$

Considering the carrier transition Hamiltonian (Eq. 4.18) in the rotating frame of laser and applying the RWA:

$$\mathcal{H} = -\hbar\delta\sigma_z + \left(\frac{\hbar\Omega_0\sigma_+}{2} \quad + \text{h.c} \quad\right) \tag{4.22}$$

We get the master equation for the case of two level system interacting with laser fields, which are known as the optical Bloch equations [15]:

$$\begin{aligned}\frac{\partial\rho_{gg}}{\partial t} &= \Gamma\rho_{ee} + \frac{i}{2}(\Omega^*\tilde{\rho}_{eg} - \Omega\tilde{\rho}_{ge})\\ \frac{\partial\rho_{ee}}{\partial t} &= -\Gamma\rho_{ee} + \frac{i}{2}(\Omega\tilde{\rho}_{ge} - \Omega^*\tilde{\rho}_{eg})\\ \frac{\partial\tilde{\rho}_{ge}}{\partial t} &= \frac{i\Omega^*}{2}(\rho_{ee} - \rho_{gg}) - \left(\frac{\Gamma}{2} + i\delta\right)\tilde{\rho}_{ge}\\ \frac{\partial\tilde{\rho}_{eg}}{\partial t} &= \frac{i\Omega^*}{2}(\rho_{gg} - \rho_{ee}) - \left(\frac{\Gamma}{2} - i\delta\right)\tilde{\rho}_{eg}\end{aligned} \tag{4.23}$$

Where we defined the phase corrected coherences: $\tilde{\rho}_{eg} = \rho_{eg}e^{-i\delta t}, \quad \tilde{\rho}_{ge} = \rho_{ge}e^{i\delta t}$.
The fluorescence rate can be calculated now, using the steady state solution which can be obtained analytically by setting the derivatives to zero:

$$\begin{aligned} F = \Gamma\rho_{ee} &= \Gamma\frac{s_0/2}{1+s_0+(2\delta/\Gamma)^2} \\ s_0 &\equiv \frac{2|\Omega|^2}{\Gamma^2} = \frac{I}{I_{sat}} \\ I_{sat} &\equiv \frac{\pi\hbar c}{3\lambda^3}\Gamma \end{aligned} \tag{4.24}$$

Where s_0 defined above is called the on-resonance saturation parameter. F is the fluorescence signal (rate of photon emission), I is the intensity, and I_{sat} is defined as the saturation intensity of the laser.

4.3 Doppler cooling

Doppler cooling was first proposed in 1975 for neutral atoms[16], and, independently, for ions[17].
Ion traps typically confine ions up to temperature of about one-tenth of their trap depth [11], which usually correspond to about 10^4K. Generally laser cooling is used to reduce this very high kinetic energy of the ion to, ideally, the ground state of the trapping potential. This is done in two stages, where only one of them will be discussed here. At first, the ion is very hot, and cooling from such high temperatures requires high scattering rate, so it is better to use a dipole transition. As mentioned above, this is typically done in the unresolved regime, since the dipole cooling transition has a short lifetime (which makes it spectrally wider than the trap frequency), using Doppler cooling method. At a later stage, a narrow transition is used to perform resolved side-band cooling to cool the ion to the motional ground state.
We'll consider a trapped ion interacting with classical laser light, which is modeled as a single traveling wave with wavevector $\vec{k}$, angular frequency $\omega_l = \omega_0+\delta$. The radiative decay time is assumed to be much shorter than one ion oscillation period ($\Gamma >> \omega_i$), which means that during one cycle of absorption and emission of a photon the ion's velocity does not change much.
Every photon absorption will give the ion a momentum kick $\Delta p = \hbar k$ in the wave-vector direction, while the emission will occur randomly to a a uniform distribution of 4π steradians - this will contribute zero momentum on average (but will result in a random walk in momentum space). The rate of absorption-emission is given in Eq. 4.24 therefore the average force applied on the ion is:

$$\frac{\mathrm{d}p_i}{\mathrm{d}t} = F_i = \hbar k\Gamma\rho_{ee} = \frac{\hbar k\Gamma|\Omega|^2}{\Gamma^2+2|\Omega|^2+4\delta_{eff}^2} \tag{4.25}$$

Since the ion is moving with some velocity with respect to the lab rest frame, it will experience Doppler shift, and so the effective detuning will be composed of detuning from resonance frequency of the ion at rest and the Doppler shift as well ($\delta_{eff} = \omega_l - \omega_0 - \vec{k}\cdot\vec{v}$).
Close to the final temperature reached, the velocities will be small (Doppler broadening small compared to Γ), thus F_i can be linearized to leading order:

$$F_i \approx F_0 + \frac{\mathrm{d}F}{\mathrm{d}v}v = F_0 + \kappa v \tag{4.26}$$

The first term is a static force (the average radiation pressure) which displaces the ion slightly from the trap center. The second term (linear in v) is a damping force with the "friction coefficient"

$$\kappa = \frac{8\hbar k^2\Omega^2\delta\Gamma}{(\Gamma^2+2|\Omega|^2+4\delta^2)^2} \tag{4.27}$$

that will provide viscous drag if its sign is negative, i.e. if the laser is red-detuned ($\delta < 0$). We can already see also that a blue-detuned laser ($\delta > 0$) will result in heating the ion. The maximal damping

is obtained for $\Omega = \Gamma$ and $\delta = -\Gamma/2$ which results in:

$$\kappa_{max} = \frac{\hbar k^2}{4} \tag{4.28}$$

This cooling process can't cool the ion to zero temperature. The reason is that at some point when the ion's energy is very low and we cannot ignore the photon recoil through stochastic emission process. The random process of momentum kicks has zero average momentum gain - $< \Delta p >= 0$, but the variance is not zero ($< \Delta p^2 > \neq 0$) - which means the momentum undergoes diffusion. Since this is a random walk process, the second moment of the distribution is proportional to the number of recoils, which we know through the excited state steady state population. The average approximate energy gain is therefore:

$$\dot{E}_h = \frac{(\hbar k)^2}{M} \Gamma \rho_{ee} \tag{4.29}$$

While the energy lost through Doppler cooling is:

$$\dot{E}_c =< F_{\text{damp}} \cdot v > \tag{4.30}$$

Equating 4.29 and 4.30, we'll get the lower bound on temperature achievable via Doppler cooling, also known as the Doppler limit (obtained for $\Omega << \Gamma$ and $\delta = -\Gamma/2$:

$$T_D = \frac{M < (v \cdot k) >^2}{k_B} = \frac{\hbar^2 k^2 \Gamma \rho_{ee}}{\kappa} \tag{4.31}$$

4.4 The Ytterbium ion

Ion trapping is not restricted to a specific specie of ions, but obtaining good coherent control is usually limited to a small group of ions. This is due to the need of robust cooling mechanisms, that can cool the ions to their motional ground state, which requires closed and fast cycling transitions. For that purpose, good candidates are the singly ionized earth-alkaline atoms which have a single electron in the outer S orbital shell, and BII transition metals as well. For quantum information purposes, generally, three types of qubits are used, optical, Zeeman and hyperfine qubits (for example [18]), and $^{171}Yb^+$ is one common selection for hyperfine qubits. For clocks and precision measurements, single Yb^+ ion has been used as well with good results [19][20][21]. The selection of an ion species determines the lasers' wavelengths. The relevant energy levels of a single-ionized Yb^+ ion is shown in figure 3. in this work we do not have (yet) the narrow clock lasers (wavelengths shown in orange), and we do not use any odd isotope, allowing us to disregard hyperfine splittings of the levels. As part of the cooling cycle, once every 200 photons scattered, the ion will decay to the long lived $D_{3/2}$ state, and also as a result of collision with background gas, it can also decay non-radiatively to the very long lived $F_{7/2}$ state. For that purpose we also deploy re-pump lasers (shown in red) to remove trapped population back to the cooling $S_{1/2} - P_{1/2}$ transition.

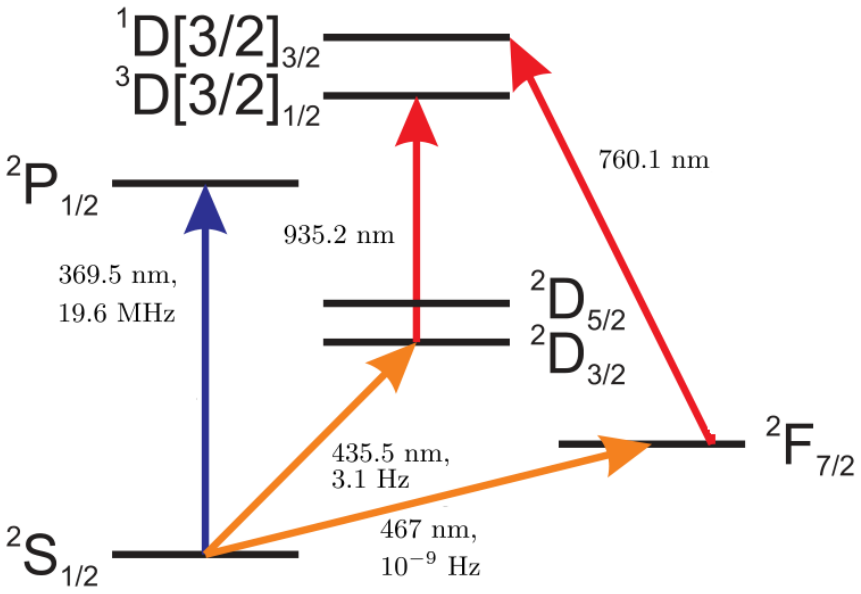

Figure 3: Energy levels of $^{176}Yb^+$ ion, adapted from [1]. The $S_{1/2} - P_{1/2}$ dipole allowed transition is marked in blue and is used for Doppler cooling and state detection as well. The transitions marked in red are "re-pumps" used to deplete population caught in the long living states, and the transitions marked in orange are the so called clock transitions, i.e., naturally narrow quadrupole or octupole transitions that can be used as frequency standards.

4.5 Photo-ionization and loading

The procedure used to load an ion to the trap involves heating a Ytterbium metal bulk to high temperatures, thus releasing a large amount of hot Yb atoms, with naturally occurring abundance as shown in table 1, to the vacuum chamber. The atoms gets ionized in a two photon process - the first one at 398.9 nm excites the atom from the ground state to the ^1P state, and the second photon at 369.5 nm (from the cooling laser), excites the electron to the continuum and ionizes the atom. The relevant level structure is shown in figure 4. This scheme allows for isotope selectivity of the ionization by tuning the 398.9 nm laser to the correct frequency.

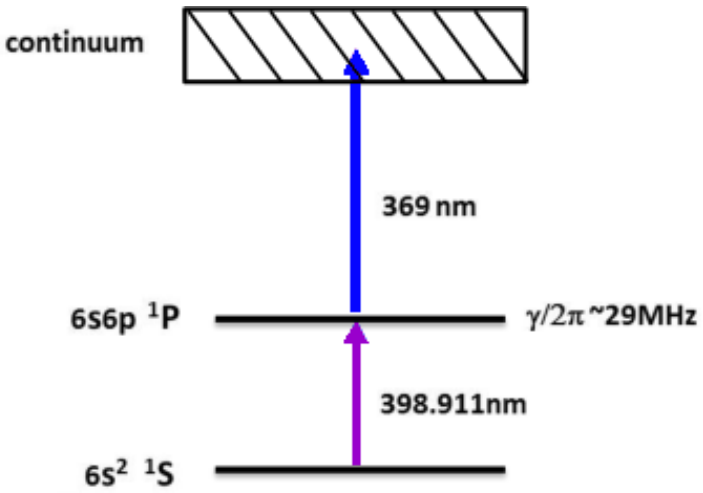

Figure 4: Relevant energy levels of Neutral Ytterbium atom.

Isotope	Natural Abundance[%]	S-P wavelength	Hyperfine Splitting [GHz]
$^{168}Yb^+$	0.13	-	-
$^{170}Yb^+$	3.04	398.91051(6)	-
$^{171}Yb^+$	13.28	398.91070(6)	12.6
$^{172}Yb^+$	21.83	398.91083(6)	-
$^{173}Yb^+$	16.13	-	10.5
$^{174}Yb^+$	31.83	398.91114(6)	-
$^{176}Yb^+$	12.76	398.91144(6)	-

Table 1: Ytterbium isotopes and their natural occurring abundance [22] and wavelength [23].

4.6 Control theory basics

Control theory deals with the control and stabilization of physical dynamic systems. It aims to regulate a noisy or disturbed system output by controlling its input. One usually differentiates "feedback" scheme, in which the control signal is generated from measurements the regulated variable itself, and "feed-forward" in which the control signal is generated from a different measurement. This work will focus on the former.

4.6.1 Linear systems

Considering a single input single output (SISO) system, with input x(t) and output y(t). A Linear Time Invariant (LTI) physical system is a system which holds two defining properties - linearity and time invariance:

- *Linearity* means the relationship between the input and output of the system is a linear map, i.e.: if $x_1(t)$ produces $y_1(t)$, and $x_2(t)$ produces $y_2(t)$, then $a_1x_1(t)+a_2x_2(t)$ produces $a_1y_1(t)+a_2y_2(t)$
- *Time invariance* means the relationship between the input and the output does not vary with time, and if we apply an input to the system now or in time T from now the output will be identical. i.e., if $x(t)$ produces $y(t)$, then $x(t-T)$ produces $y(t-T)$.

Recalling the Laplace transform defined as:

$$\mathcal{L}[x(t)] \equiv X(s) = \int_0^\infty x(t)e^{-st}dt \tag{4.32}$$

Thus, an n-th order linear differential equation transforms into an n-th order algebraic equation in s [24]. This allows us to define a transfer function, G(s), for LTI systems, which are described by linear differential equation as:

$$G(s) = \frac{Y(s)}{X(s)} \tag{4.33}$$

For LTI systems, compound of two systems are described by convolution in time-domain, which is, according to the convolution theorem, simply multiplication in Laplace domain ($\mathcal{L}[G * H] = G(s)H(s)$). This motivates the introduction of block diagrams that represent the flow of signals for linear systems, one such example of an open loop system containing system dynamics G(s) and sensor response H(s) is shown in figure 5.

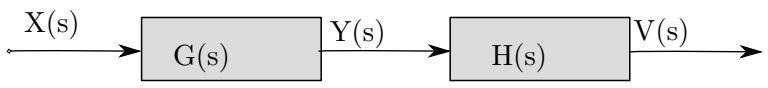

Figure 5: Block diagram illustrating signal flow from the input X through the system dynamics G to the output Y. The signal then flows through the sensor H to the measured value V.

Consider a system whose dynamics are described by G(s). The goal of a control system is to have the system's output y(t) follow some control signal r(t) as faithfully as possible. The general strategy consists of two parts: First, we measure the actual output y(t) and determine the difference between it and the control signal, generating the error signal $e(t) \equiv r(t) - y(t)$. The we apply some "control law" K to the error signal to try and minimize its magnitude. An example for such a system following this general scheme with outside disturbances d(t) and measurement noise $\xi(t)$ added is displayed in figure 6.

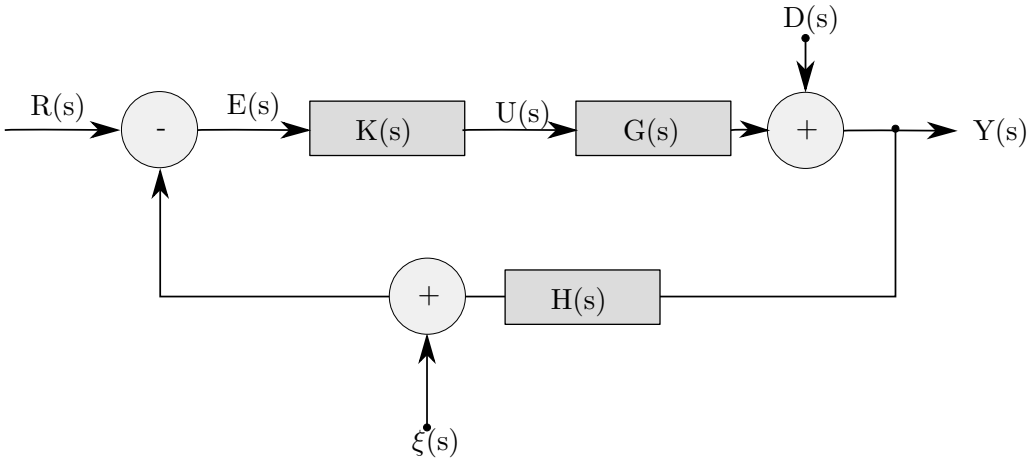

Figure 6: Block diagram illustrating closed-loop control of a system G(s), subject to disturbances D(s), through sensor H(s) with measurement noise $\xi(s)$. Controller dynamics are described by K(s). The control signal is given by R(s).

From the block diagram in figure 6, it is easy to determine that $Y(s) = K(s)G(s)E(s) + D(s)$, and since we defined the error signal as $E(s) = R(s) - (Y(s)H(s) + \xi(s))$, we'll get the relation between the output and the control signal and noise (the closed loop dynamics):

$$Y(s) = \frac{KG}{1 + KGH}[R(s) - \xi(s)] + \frac{1}{1 + KGH}D(s) \tag{4.34}$$

Now we can use this very general scheme, to analyze some basic properties of feedback systems. Firstly, let's consider the case where there is no measurement noise, i.e, $\xi = 0$. In such a case, we can clearly see in eq. 4.34 as the loop gain (defined as $L(s) \equiv K(s)G(s)$) gets larger, the output tends to track the control signal better while increasingly rejecting disturbance ($K(s)G(s) >> 1 \Rightarrow Y(s) \approx R(s)$). System stability should also be taken into account when designing such a control system, as the higher the gain the more the systems tends towards instability.

Secondly, let's consider a system with measurement noise, but no non-trivial measurement dynamics (H=1). We can also already see one the most common trade-offs in designing a control system, high gain would increase the feedback bandwidth which would help reject disturbances (as mentioned above). On the other hand, the control signal effectively becomes $r - \xi$ (the system has no way to distinguish the control signal from the measurement noise). Thus the higher the gain the more the measurement noise is amplified as well. This trade off may also be expressed by re-writing eq. 4.34 as:

$$\begin{aligned} E_0(s) &= R(s) - Y(s) = S(s)[R(s) - D(s)] + T(s)\xi(S) \\ T(s) &\equiv \frac{KG}{1 + KG} \\ S(s) &\equiv \frac{1}{1 + KG} \end{aligned} \tag{4.35}$$

Where we defined here the tracking error, $E_0(s)$, i.e., the difference between the control signal and the actual output (as opposed to E(s) which is the difference between the control signal and the measured

output). In eq. 4.35 we also defined two functions, S(s), known as the sensitivity function, and T(s), known as the complementary sensitivity function, because $S(s) + T(s) = 1$ at all frequencies. This is a fundamental obstacle, which reads - if S is small and disturbances are rejected, then T is large and sensor noise feeds through, and vice versa.

4.6.2 Discrete PID controller

Probably, one of the most common forms for K(s) is the PID controller, which is a combination of proportional, integral and differential control. The control dynamics in time domain and frequency domain are:

$$\begin{aligned} u(t) &= K_p e(t) + K_i \int_0^t e(t')dt' + K_d \frac{\partial e(t)}{\partial t} \\ K(s) &= \frac{U(s)}{E(s)} = K_p + \frac{K_i}{s} + K_d s \end{aligned} \tag{4.36}$$

Choosing these parameters, K_p, K_i and K_d can be done in all sorts of different ways, with many methods from manual tuning to more analytical existing in the different literature.
In this work, and also very common today in most realizations, the control system is implemented digitally, and once needs to be careful when moving from continuous to discrete systems. Firstly, when moving to digital systems, the input signal must be low-pass filtered to avoid aliasing, according to the Nyquist sampling theorem. Effects of aliasing in time-domain and frequency domain, when no such filtering is done, is presented in figure 7, adapted from [24].

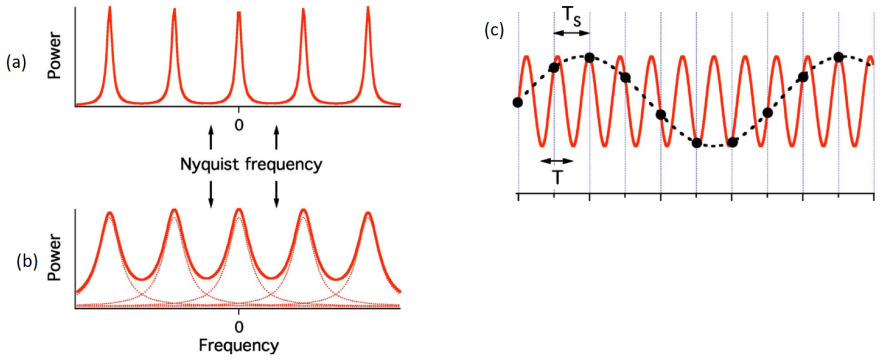

Figure 7: Effects of aliasing in frequency and time domain. (a) shows a sampled signal where the maximum frequency of the power spectrum of the continuous signal is less than the Nyquist frequency. The sampled spectrum faithfully represents the continuous one. In (b), the maximum frequency excess the Nyquist frequency, resulting in aliased spectra overlap, distorting the estimation of the continuous spectrum. (c) shows this effect in time domain, where a high frequency continuous signal (solid curve) is sampled at a larger sampling period (T_s) than needed by the Nyquist criterion. The apparent measured points (large dots) are interpreted as resulting from a much lower frequency signal (dashed curve).

The common tool to analyze discrete systems is called the "Z transform" and is derived by introducing the variable $z = e^{sT_s}$ to the Laplace transform of a sampled signal with sampling period T_s [24]:

$$\mathbb{Z}[f] = \mathcal{L}[f_s(t)]\Big|_{z=e^{sT_s}} = \mathcal{L}\left[\sum_{n=0}^{\infty} f(t)\delta(t - nT_s)\right]\Bigg|_{z=e^{sT_s}} = \sum_{n=0}^{\infty} f_n z^{-n} \tag{4.37}$$

Using the non-symmetric approximation for the derivative and the Trapezoidal method for estimat-

ing the integral, we can approximate the derivative and integral, in time domain:

$$\begin{aligned}\frac{\partial y(k\cdot T_s)}{\partial t} &\equiv D[k] \approx \frac{y[k]-y[k-1]}{T_s}\\ \int_0^{k\cdot T_s} y(t)dt &\equiv I[k] \approx I[k-1] + \frac{y[k]+y[k-1]}{2}\cdot T_s\end{aligned} \tag{4.38}$$

The Z-transform has the well known time shifting property:

$$\mathbb{Z}\{x[k]\} \equiv X[z] \quad \Rightarrow \quad \mathbb{Z}\{x[k-n]\} = z^{-n}X[z] \tag{4.39}$$

Using equations 4.39 4.38 and substituting in the PID controller, we get the approximate discrete transfer function of a PID:

$$\begin{aligned}K[z] = \frac{U[z]}{E[z]} = K_p + K_i\frac{T_s}{2}\frac{z+1}{z-1} + K_d\frac{z-1}{zT_s} =\\ = \frac{\left(K_p + K_i\frac{T_s}{2} + \frac{K_d}{T_s}\right)z^2 + \left(-K_p + K_i\frac{T_s}{2} - \frac{2K_d}{Ts}\right)z + \frac{K_d}{T_s}}{z^2 - z}\end{aligned} \tag{4.40}$$

Re-arranging eq. 4.40 and transforming back to time domain, we'll get the simple implementation of digital PID controller:

$$\begin{aligned}u[k] &= u[k-1] + ae[k] + be[k-1] + ce[k-2]\\ a &= \left(K_p + K_i\frac{T_s}{2} + \frac{K_d}{T_s}\right)\\ b &= \left(-K_p + K_i\frac{T_s}{2} - \frac{2K_d}{T_s}\right)\\ c &= \frac{K_d}{T_s}\end{aligned} \tag{4.41}$$

5 Experimental setup

5.1 Trap design

5.1.1 Geometric configuration

As discussed in subsection 4.1, in order to control the trap parameters a_i and q_i one needs to apply both DC and RF voltages in a fashion compiling with eq. 4.3. Some considerations taken while designing the traps are the optical access for lasers and imaging, the distance between the electrodes and ions and bias and compensation voltages. The final design is shown in figure 8.

Optical access. The use of laser cooling requires one to apply a laser field with $\vec{k}$ having components on all primary axes of motion in the trap, while optical pumping schemes require aligning the re-pump laser with the magnetic field (quantization axis). State detection is done via imaging of spontaneous emission, requiring another optical access line with as high as possible numerical aperture. Lastly, for best isotope selectivity while loading ions, it is preferable that the ionization beam (399 nm) will be as perpendicular as possible to the oven emitting very hot atoms, in order to reduce the Doppler broadening of their absorption spectra as much as possible.

The distance to near electrodes, denoted d_0, is the single most important parameter defining the ratio between the applied voltage and the resulting potential interacting with the ion. As a result, this also affects the trap secular frequencies, which has many implications on cooling, manipulation and detection. Secular frequencies scale as $\sim 1/d_0^2$, and the typical secular frequencies are a few MHz. In order to achieve this with less than 1kV applied to the RF and DC electrodes, the distance to the x-y plane electrodes should be kept no larger than ~ 1 mm.

Bias voltage and all axes compensation. According to 4.3, the middle DC electrodes in our segmented DC electrodes should be grounded, resulting in a degeneracy of the radial modes - from symmetry of the design the x and y secular frequencies will be the same. This doesn't enable efficient laser cooling, and thus this degeneracy needs to be lifted. This is done by using the middle bias electrode which is typically set to just a few volts. Lastly, as explained in 4.12, stray fields cause excess micro-motion which does not scale down with the ion temperature, and we need to allow correction in all 3 axes. The axial direction is compensated by applying a differential mode the end caps and similarly, the DC direction is compensated with differential mode applied to the bias electrodes. This is not easily done the same way to the RF electrodes, and to allow compensation in the RF axis, another electrode is added at the bottom of the trap (RF Compensation in figure 8).

Lastly, a grounded electrode is added at the bottom of the trap, allowing us to drive AC current, which results in AC magnetic fields being applied to the ion, this can be used with RF and MW fields to couple between Zeeman and hyperfine levels of the ion.

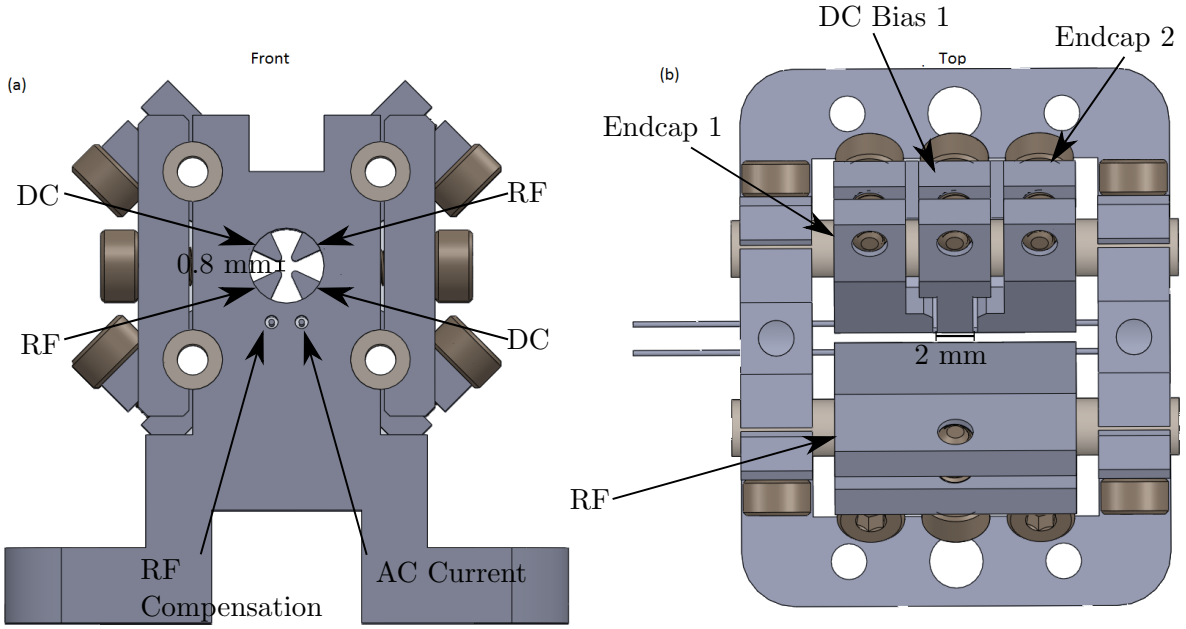

Figure 8: Trap design. (a) shows a view from the front, the design was made such that optical access is available along the trap axis. (b) shows a view from the top and the dimensions of the trap center.

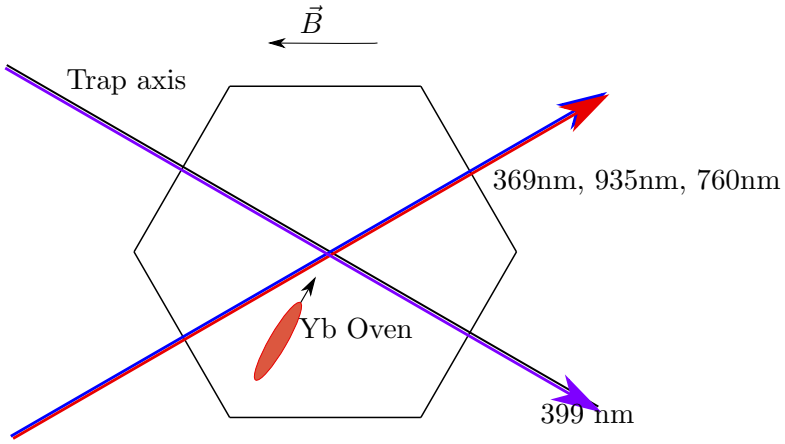

Figure 9: Laser beam orientation inside the trap

Figure 9 shows the optical configuration of the trap, with the imaging axis directed along the axis perpendicular to the page. The ionization beam is applied as perpendicular as possible to the oven, to reduce Doppler broadening. The re-pump lasers are currently not applied through the quantization axis, as for this work no optical pumping is needed.

5.1.2 Electronic circuit

Reaching the desired secular trap frequencies of few MHz requires applying very high voltage (hundreds of volts) to the RF electrodes at a frequency of tens of MHz. Common RF amplifiers does not reach such high voltages, and moreover they are not designed to match the high impedance of the RF electrode to the ground (caused by the very small capacitance between the electrode and the ground). For this purpose a helical resonator is used which amplifies the input voltage while performing the required impedance matching. The resonator used in this work has a measured Q factor of $\sim$ 500, and a measured center frequency of 18.85 MHZ. The helical resonator couples RF power from the amplifier into the trap, by a small wire loop inside a cylinder. Energy is coupled via magnetic field produced by the current running in the loop, inducting current on the cylinder. A comprehensive discussion and design guidelines can be found in [25]. Between the amplifier and the resonator a (reversed) directional coupler is inserted, allowing for reflections from the resonator to be monitored by an oscilloscope, then the coupling of the RF power can be optimizing by slightly adjusting M_R (moving the coils), and the RF frequency and trying to minimize the reflections from the coupler.

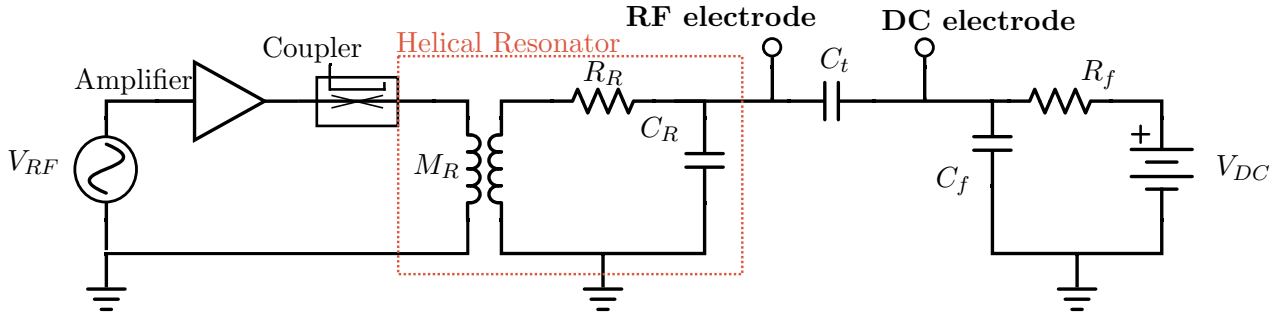

Figure 10: Schematic diagram of the electronic RF and DC circuits.

Connecting each of the mentioned DC electrodes is done through an high capacitance (C_f) low-pass filter as shown in Figure 10, to overcome parasitic capacitance coupling between the RF electrode and the DC electrode (denoted C_t) and keep the DC electrode close to the RF ground, it also helps isolate the DC source from the RF. Since the approximate capacitance for our geometry is in the order of $C_t \sim pF$, A capacitor of $C_f = 220nF$ was chosen, suppressing the RF voltage with about 5-6 orders of magnitude from the DC electrodes. The resistor R_f was chosen accordingly, as $R_f = 1k\Omega$, amount to about 700 Hz bandwidth (far from trap secular frequency) of the low-pass filter , to filter DC source noise - Assuming trap secular frequencies are at the order of 1 MHz, we'll get approximately 60 dB attenuation of the noise at that frequency.

5.2 Laser systems

Semiconductor diode lasers have found wide variety of applications in a very broad range of fields, atomic physics being one of them, due to their considerably lower cost, small size, high reliability and more, as compared to the traditional tunable dye or Ti-Sapphire laser. Diode lasers are basically forward biased p-n junctions, in which charge carriers flow through the junction, due to the voltage applied, then they recombine, emit radiation and produce the required population inversion between the conductance and valence energy bands. The other requirement for lasing, the optical cavity, is created between the facets of the diode itself, the back facet is coated with highly reflected material

while the front facet is usually uncoated and reflects due the Fresnel reflections (difference in index of refraction between the semi-conductor and the air).

Typical diode lasers size is in the mm range, resulting in Free Spectral Range of $FSR = c/2L \sim 100$ GHz (where L is the cavity length and c is speed of light), whilst the gain profile of a semiconductor is usually very wide (several nm - spanning multiple cavity modes). This results in multiple longitudinal modes lasing simultaneously, and also each mode is very wide (tens of MHz) due to its low finesse and small size.

Thus, unmodified, the diode laser's frequency tuning, linewidth and optical spectrum (multi-mode) are far from ideal, which greatly reduces their utility. These characteristics can be improved by the use of optical feedback to control the wavelength of the laser. There are some possible techniques to do so, one popular approach is by the use of an external cavity diode laser (ECDL) [26].

5.2.1 External Cavity Diode Laser

To overcome this shortcomings, it is possible to put the diode laser (with or without anti reflection coating on its output facet) inside an external cavity, with some frequency-selective optical feedback to the diode. One common configuration, which is used in this work, is called the "Littrow" configuration, and it consists of the diode laser, a collimating lens and a diffraction grating, from which the first-order diffracted light is fed back to the diode, while the directly reflected light forms the output beam [27], this configuration can be seen in figure 11.

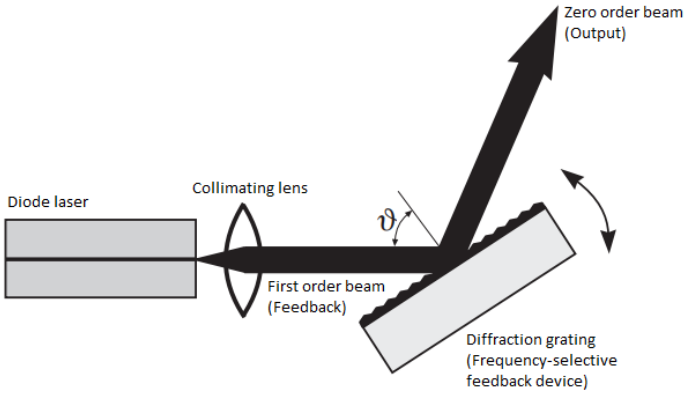

Figure 11: Schematic diagram of an ECDL in Littrow configuration. Adapted from [28]

Incident beam at angle θ will be diffracted from the grating according to the grating equation:

$$m\lambda = d(\sin\theta + \sin\theta') \tag{5.1}$$

Here, m is the order of the diffraction, λ is the wavelength, d is the distance between adjacent grooves on the grating and θ' is the wavelength dependent reflection angle. In Littrow configuration, the first order ($m = 1$) reflected beam is fed back to the laser ($\theta' = \theta$), resulting in:

$$\lambda = 2d\sin\theta \tag{5.2}$$

The result is the output laser beam has usually only one longitudinal mode - due to the wavelength selectivity of the grating acting as a spectral filter and narrowing the gain profile to be much smaller. Moreover, the significantly larger dimensions of the external cavity (few cms), reduces this mode linewidth to be about 1 MHz or even less.

5.2.2 ECDL design

Our own ECDL design is shown in figure 12. Unlike common designs, there is no piezoelectric actuator used to stabilize the grating angle, it is fixed once and then tightened well with the screws. Stabilization will only use current and temperature. Grating used are Thorlabs' holographic gratings, where the distance between the grooves is chosen according to the wavelength, such that the output angle (eq. 5.2) will be about the same (about 20 degrees in this case), allowing us to create the same casings for all of our lasers, this happened to be 2400 grooves/mm for the UV/blue lasers and 1200 grooves/mm for the IR/red lasers.

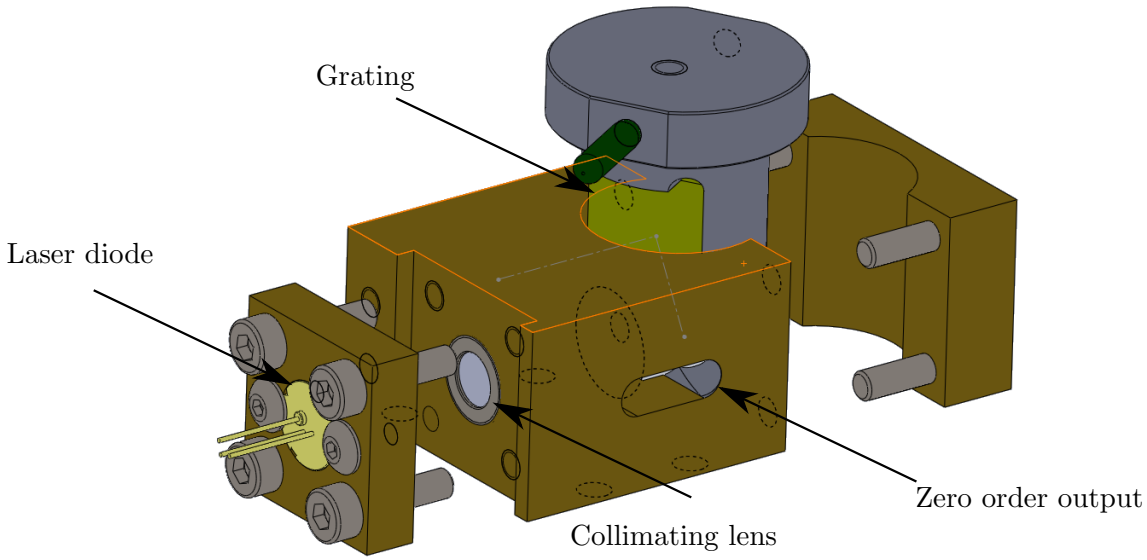

Figure 12: ECDL design used in this work, without any PZT.

5.2.3 Wavelength tuning

There are a few ways to tune the wavelength of an ECDL, each with its own characteristics of timing and bandwidth

Grating angle The first parameter that can be adjusted is the grating angle, which changes the wavelength which is fed back to the diode laser according to eq. 5.2. This is very coarse tuning, and in practice this is almost never adjusted after the first initial setup, only temperature and current are used for daily set-point configuration. The technique used to properly align the grating angle uses the fact that laser operation is characterized by a liner PI curve (power as a function of current) above some threshold and almost zero power below the threshold. Feeding back laser power to the diode, results in a PI curve which has smaller slope (some of the power is used for feedback), but lower threshold current (see figure). Thus, by setting the current to just above the threshold current and then slowly changing the grating angle will result in a very very small angle ranges in which the output power gets larger considerably, when the cavity is closed and the laser is fed back exactly to the diode. This phenomenon is called "flash", and it is usually visible with naked eyes.

Temperature There is an approximate linear relationship between temperature and center wavelength for diode lasers (typical coefficients are $\sim 0.03\, nm/^{\circ}K$), this occurs due to thermal expansion

of the diode which changes the cavity length. Therefore the temperature is stabilized as explained in 5.2.4, and the controller set point is tuned, alongside current, to achieve the desired frequency. This parameter allows for changes over a large range of frequencies, but it is difficult to make small changes in, thus useful for coarse tuning (less than grating, more than current). Also, the time for temperature change to occur and stabilize is very long, and so it cannot have a large enough bandwidth for stabilization.

Injection current alters the lasing chip temperature via Joule heating, and thus has a similar linear relationship to the wavelength. Unlike external temperature control which heats / cools the large bulk housing of the ECDL, injection current raises the temperature internally inside the diode itself and so it allows for much faster and more accurate tuning, alas over a small possible range, leaving it as the finer tuning used after temperature and grating angle were set. The current also increases the carrier density withing the lasing medium, affecting the refractive index, but above the threshold current the carrier density is clamped and this effect gets negligible, leaving only the thermal mechanism at low frequencies (below $\sim$1 MHz). For current stabilization and set point adjustment we use an analog current driver circuit designed in BYU[29][30].

Mode Hopping Figure 13 depicts typical temperature dependence of the wavelength, it shows non-continuous regions with linear dependence. This non-continuity is called a mode hope, and it appears when the peak of the gain medium has shifted too far in the tuning process, that a different longitudinal mode lases instead. This figure is shown for temperature dependence but the current dependence shows the same mode hop phenomenon, thus its true to look at a 2D stability region maps of temperature and currents. For this reason, while tuning the laser wavelength, adjustments needs to be made simultaneously for temperature and current.

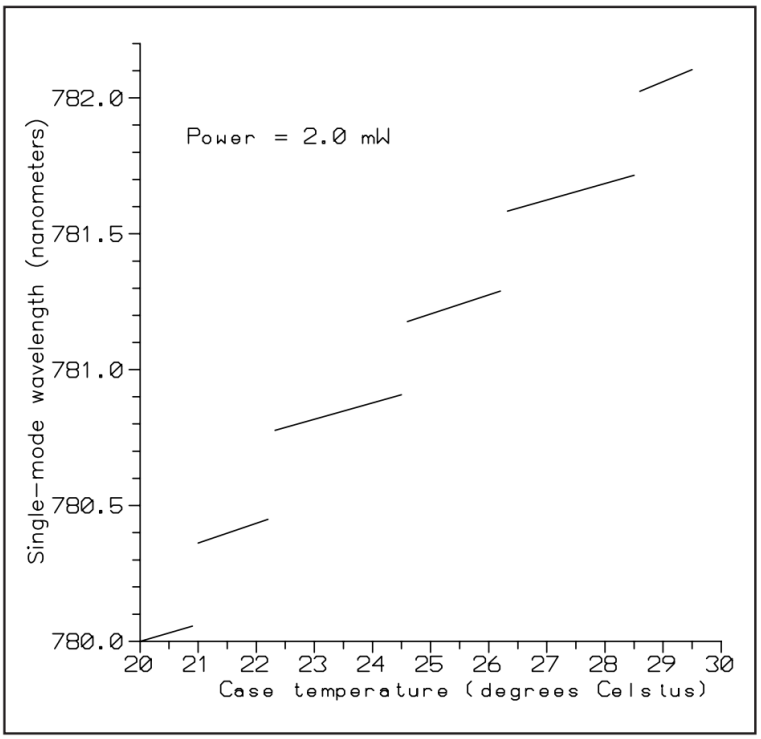

Figure 13: Temperature dependence of single-mode wavelength of a diode laser at constant power. Taken from Newport's application note [31].

5.2.4 Temperature stabilization

Stabilization of temperature is performed using a digital PID control system implemented in Arduino uno, as explained in section 4.6.2. The temperature is measured using a self-built circuit, measuring the resistance of a Thorlabs' TH10K thermistor relative to some reference resistor (chosen to be $11.5k\Omega$ for most lasers), using Texas Instruments' ADS1148-Q1 16-bit Analog-to-Digital Converter (ADC) with integrated programmable gain. The Arduino's digital output is converted to analog voltage using a DAC, and then fed into a Thorlabs' Thermoelectric cooler (TEC3-2.5).
With the settings we used of $V_{ref} = 2.05V$, gain $= 32$, the measurement is performed with a full-scale range of $\sim 2.9k\Omega$ and an LSB of $\sim 4.4\Omega$. The thermistor temperature dependence is not linear but in a small range can be approximated as linear, which gives corresponds to a full-scale range of $\sim 5.6°K$ and an LSB of $\sim 85\mu K$.
A typical temperature tuning coefficient is $15GHz/°K$, which means that the best frequency resolution that can be achieved due to temperature control is roughly $1.30MHz$. The in-loop measurement (the signal being stabilized) of the ADC is shown in figure 14, while the un-stabilized measurement is shown in figure 15.

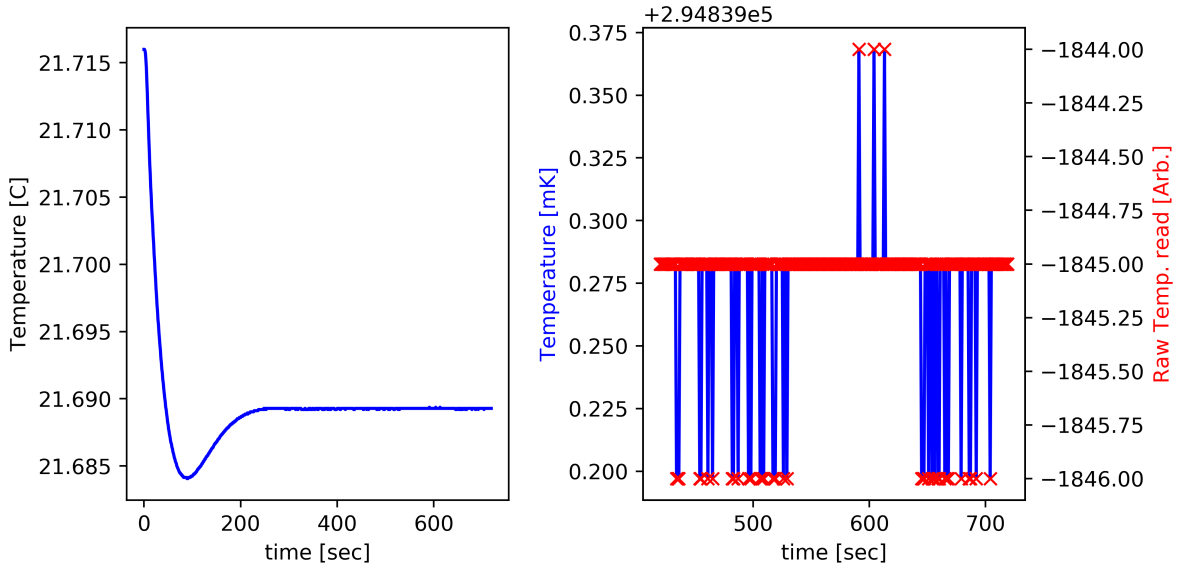

Figure 14: Stabilized temperature of the 935nm ECDL's case. On the left the transient response for setpoint change is shown, while the right deceits the steady state measurements (zoom in of the last 5 minutes) - where the quantization effect of the stabilization is apparent.

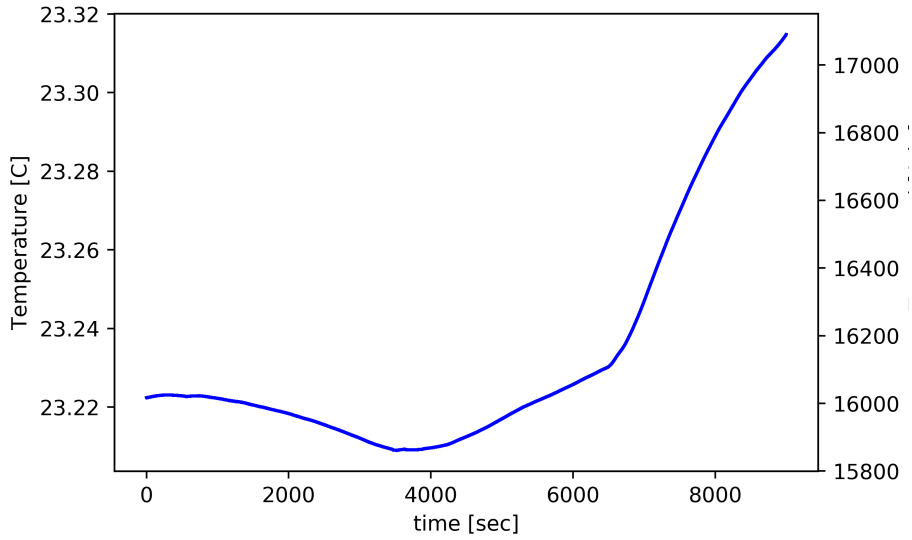

Figure 15: Free running temperature of the 935nm ECDL's case.

5.2.5 Stabilization

The noise spectrum of the laser's frequency leads to an effective linewidth which can be though of as broadening of the laser's spectrum around its central frequency[32]. From this treatment, we can see that the laser linewidth is dependent on the timescale over which it is evaluated, and typically a laser can contain very different fast and slow components. Thus usually, one describes the linewidth as the "fast" fluctuation (faster than the spectroscopic interaction time, typically tens or hundreds of microseconds, a few milliseconds in our case), and the low-frequency fluctuations cause jitter of the central spectral line in frequency space. Locking the laser can reduce the linewidth and also suppress drift over time.
Stabilization of a laser (or laser locking) means keeping its frequency fixed to an external frequency reference, i.e., reducing the frequency fluctuations between the laser and the reference. It revolves generating some error signal with respect to the reference, feeding it to some electronic control circuit (digital or analog) and feeding the output back to the laser, where common references usually used are Fabry-Perot cavities, atomic transitions and more.
In this work, no ultra-narrow lasers are needed, so a digital feedback system was created (slower than analog circuits, but much easier to implement and adjust), using a WS30 HighFinesse wavelength meter as a frequency reference. Since the same wavelength meter is used for all 4 lasers (and also 4 more from our $^{88}Sr^{+}$ experiment), a system for time multiplexing the different lasers composed of 2 Acostu-Optic Tunable Filters (AOTF), 8 DDS and dichroic mirrors was built. The computer sends the relevant RF signal to the filters deciding which wavelength will arrive at the wavemeter, perform the measurement and continuing to the next laser, as shown in figure 16. The current which is a high loop bandwidth (fast response), is used to stabilize the frequency to the desired setpoint using a digital PID controller. When current modulation gets too large, usually the diode mode hops, and the laser lock breaks, to compensate for that, a second low bandwidth digital PID was added, which tries to minimize the current modulation via temperature modulation.

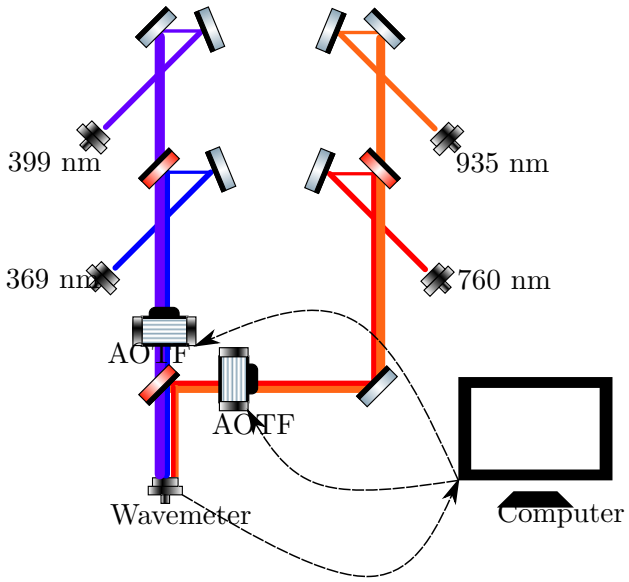

Figure 16: Wavemeter switch used in this work to stabilize 8 lasers to a single Highfinesse wavelength meter.

As mentioned in 5.2.2, the two parameters used to set the wavelength are temperature and current, and both are used for stabilization as well, in a 2 feedback loops control system, shown in figure 17.

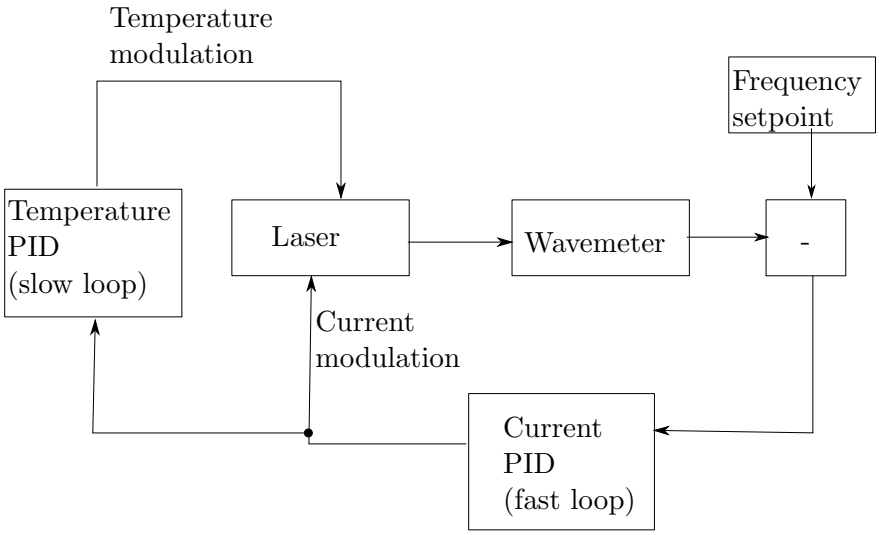

Figure 17: Laser frequency stabilization feedback system, consists of 2 loops. The fast one stabilizes the laser frequency to about 1 MHz using current modulation. The current modulation output itself is then fed back to a slow loop which modulates the temperature, trying to minimize current modulation. This scheme allows for the lock to run for a considerable amount of time before mode hops due to current modulation gets too large.

The stabilization result is shown in figure 18. In both the free running (blue) and locked (red) signals, temperature is stabilized.

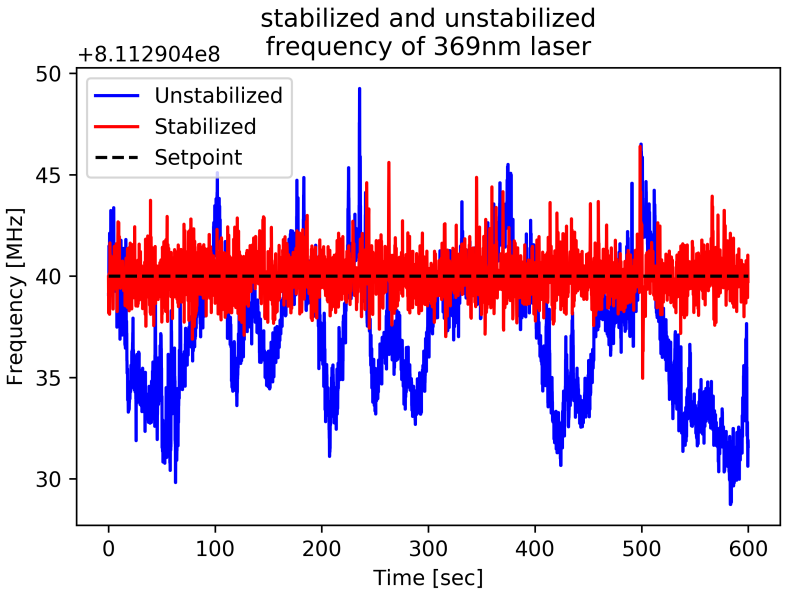

Figure 18: Ten minutes of in-loop frequency measurements of 369nm laser using the wavelength meter. Stabilized signal is in red and free running in blue, while the black dashed line is the frequency setpoint for stabilization.

5.2.6 Beam lines

All graphical components are taken from [33].

369 nm For Yb^+ ion's 369.5nm $S_{1/2} - P_{1/2}$ transition ($\Gamma/2\pi = 19.6MHz$), according to Eq. 4.24: $I_{sat} = 8.08\left[\frac{mW}{cm^2}\right]$. The calculated beam waist of the 369 beam on the ion is approximately $60\mu m$, resulting in $P_{sat} = 0.2\mu W$. In this experiment we shine the 369 laser with power of about 6 μW, resulting in $s_0 = P/P_{sat} \approx 30$.
The laser is transmitted to the ion through a Brimrose TEF-150-100-370 Acousto Optic Modulator (AOM) in a double pass configuration, allowing to scan very quickly the laser frequency in almost 200 MHz range, which can be used both for off-resonance and on-resonance cooling, as well as acquiring the absorption spectrum for this transmission.

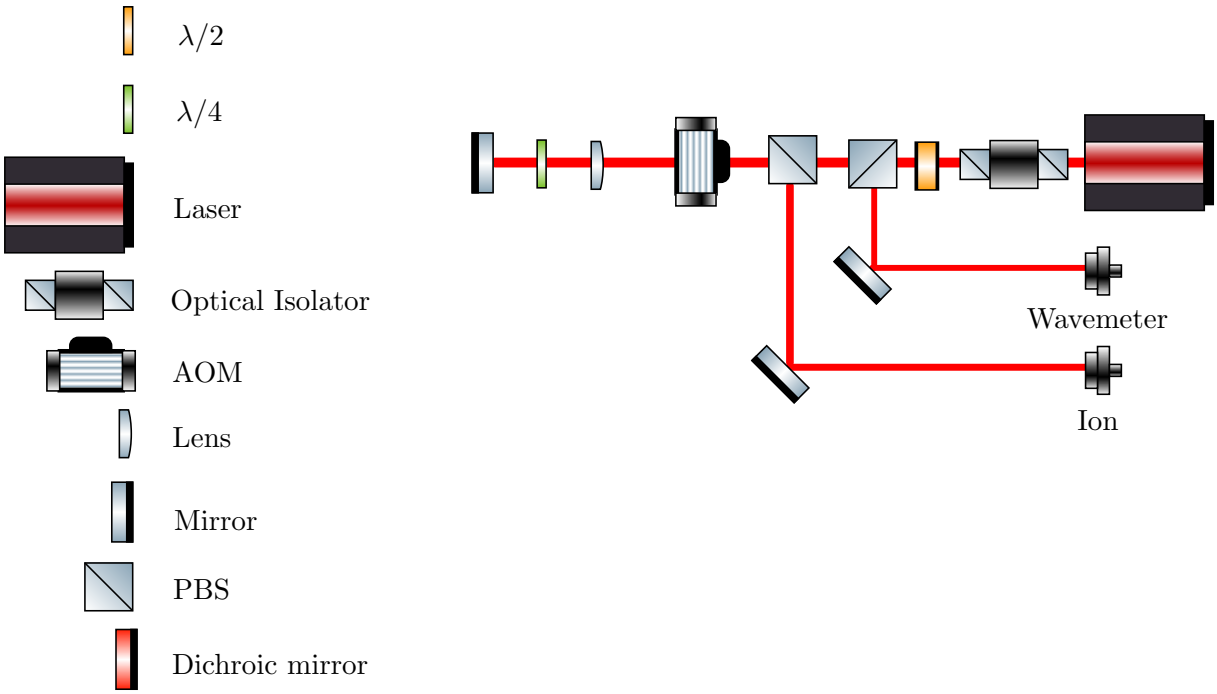

Figure 19: Beam line for the 369 ECDL

399 nm For the natural Yb $S_1 - P_1$ transition, a laser tuned to 389.9 nm was used, stabilized to the wavelength corresponding to the desired isotope, according to table 1. The output power received is about 20 μW, and is focused to a calculated beam waist of about 100 μm as well.

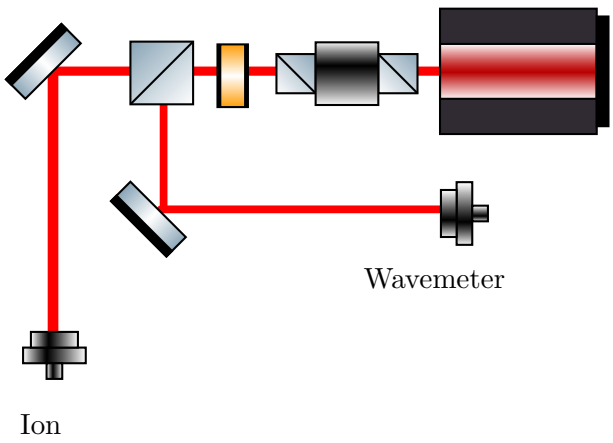

Figure 20: Beam line for the 399 ECDL

760 and 935 nm For the re-pump lasers, both are jointly coupled to a single fiber going into the trap, but independently going to the wavelength meter switch for stabilization of the desired wavelength. The 760 nm output power is about 300 μW focused to a calculated beam of about 80 μm, while the 935 nm output power is about 1 mW focused to about 100 μm beam.

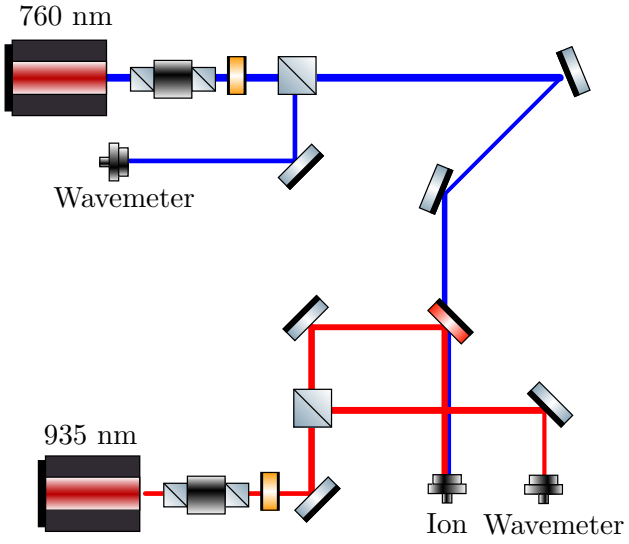

Figure 21: Beam line for the 760 and 935 ECDLs

5.3 Imaging system

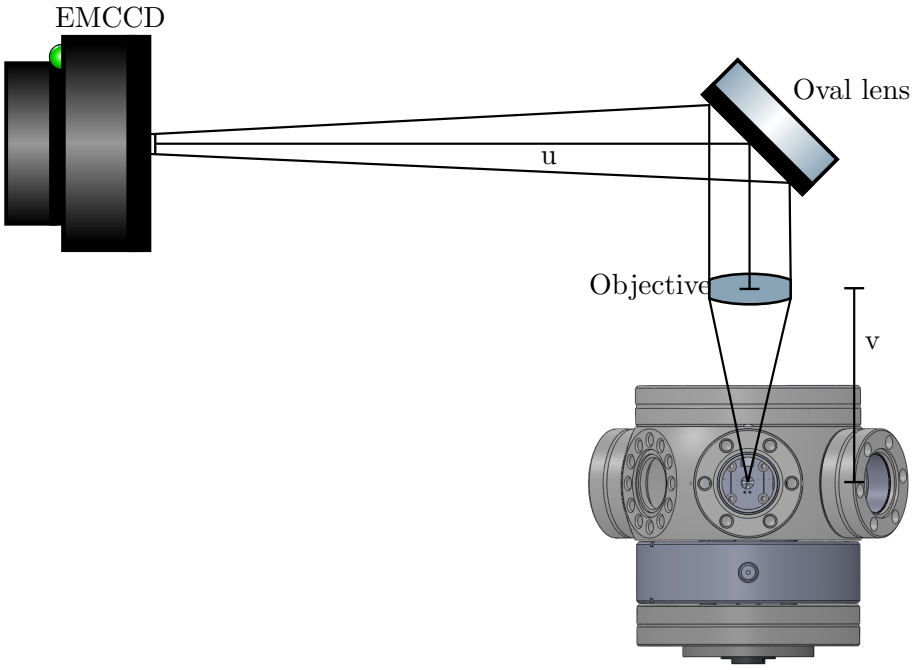

Figure 22: Imaging system used for fluorescence detection

The imaging system used to view the ion fluorescence is shown in figure 22. It is composed of an objective with a working distance of about 3.7 cm, and a Numerical Aperture (NA) of approximately 0.32, an oval lens and an Electron-Multiplying Charge Coupled Device (EMCCD) camera. The camera used is Andor Luca S 658M, which provide quantum efficiency of about 40% in the required wavelength and x200 EM gain.

The diffraction limit of a single very small emitter (like a trapped ion), is defined (according to

Abbe criterion) as the radius of the formed Airy disk:

$$r = 1.22\frac{\lambda}{NA} = 1.22\frac{369.5nm}{0.32} \approx 1.15\mu m \tag{5.3}$$

This is the minimal distance between objects that will be distinguishable in a diffraction limited system. Our camera is positioned about 25 cm from the lens, and the ion is imaged onto our camera with a magnification that is determined by the distance from the camera to the lens, in the following manner:

$$\begin{aligned} \frac{1}{f} &= \frac{1}{v} + \frac{1}{u} \quad \Rightarrow v = \frac{uf}{u-f} \\ M &= \frac{u}{v} = \frac{u-f}{f} \approx 5.67 \end{aligned} \tag{5.4}$$

where u is the distance from the lens to the camera, v is the distance from the lens to the object, and f is the lens focal length.
Since the size of a single pixel in the Luca camera is 10x10 μm, the ion is expected to be projected to about 1 pixel in the final image. This is usually not wanted, and we plan on distancing the camera further from the system in order to enlarge the magnification.

5.4 Vacuum system

Trapped ions require Ultra High Vacuum (UHV) systems, in order to avoid, as much as possible, collisions with the background gas atoms. These collisions usually do not kick the ion our of trap due to its large depth, but it can certainly heat the ion and from time to time change its internal state damaging the results (in Yb^+, for example, it can cause non-radiative decay to the very long lived F state). Also, in certain species, chemical reactions can occur between the ion an the surrounding hydrogen resulting in a stable molecule and a need to load a new ion instead (in Yb^+ this is less common than other species). Luckily, UHV is a commercially available technology, and reaching as low as a few 10^{-11} Torr is possible (alas, not easy) with correct material choice and design. The vacuum system used here is composed of the following parts: chamber, vacuum pumps, valve, viewport windows and electrical feedthrough, and is displayed in figure 23.

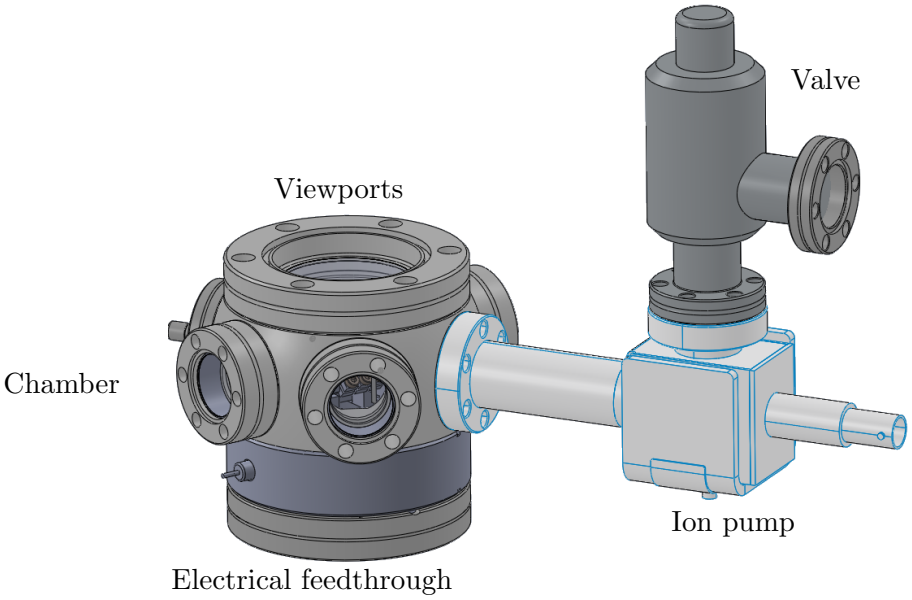

Figure 23: Vacuum system components

The chamber used is a Kimball 2.75" Spherical Hexagon vacuum chamber, with internal volume of about 74 cc. The top facet has a 2.75" CF viewport used for the imaging system, the bottom is used for an electrical feedthrough to the trap, and out of the 6 side facets, 4 has optical viewports installed for laser input, one facet has the ion pump connected and the last one have the RF input from the helical resonator.

5.4.1 Pumps

The pumps role is to actively pump out gas from the chamber to reduce its pressure. Three types of pumps are used in our system, each with its own use.
Initially, a mechanical HiCube 80 Eco pump was used, it is composed of a diaphragm pump and a turbo-pump as well. It is well suited for high pressures going down from 1 atmosphere to about 10^{-6} Torr, and then it becomes inefficient. Moreover, mechanical pumps induce large vibrations which could interrupt the experiment, therefore the mechanical pump is used for the first stage, until 10^{-6} Torr is reached and then the valve is closed and the pump is disconnected.

Ion pump ionizes the gas with a cloud of swirling electrons confined in a strong magnetic field. It also employs a strong electrical potential, typically 3-7 kV, which causes the ionized gas to accelerate into and be captured by the solid electrode. Ideally, ion pumps can reach pressures of down to 10^{-11} Torr, but cannot start at 1 atmosphere, thus they are used as a second step after mechanically pumping first. The ion pump used in this work is Gamma Titan 3S.

NEG Non-Evaporable Getter (NEG) pump is made of various alloys which chemically absorb gases (mostly porous allows or powder mixtures of Al, Zr, Ti, V and Fe). Once absorbed, the gas atoms create strong chemical bonds, and thus not easily removed, thus this pump has a finite capacity. It is possible to activate it by heating it (usually by driving current in resistive heating wires), thus removing the passive or saturated surface layer of the NEG. The NEG used in this work is SAES Getters' ST172/NP/TI/HIT-L/16-10/300C.

5.5 Ytterbium Oven

As explained in 4.5, loading the trap with Yb ions, involves vaping atoms from a bulk of solid Ytterbium. In room temperature the vapor pressure is much too low to sufficiently load ions, and thus one needs to heat the sample. For best efficiency for the loading, a control oven the size and direction of the atomic beam is needed, and it is done by creating an oven for the Yb. This is done by taking a stainless steel tube of about 1 mm diameter, and clipping one side of it, then 2 stainless wires are point welded to both ends of the tube, allowing for current to flow through the tube and heat it (an improvement in heating is possible with much lower current, if a resistive heater is used adjacent to the tube, instead of driving the tube itself). The oven then gets filled with a bulk of Yb solid, and is placed inside the chamber, approximately 2 cm from the trap, as perpendicular as possible (to reduce Doppler broadening of the neutral S-P transition, and allowing better isotope selectivity while loading). It is better to try and shorten the time between exposing the Yb to the air and sealing the vacuum, to avoid oxidation as much as possible.

The oven was then checked by shining the 399 nm laser near the output of the oven while driving current, and looking for fluorescence from the atoms. In our trap, fluorescence is visible with bare eyes at about 190-200 mA drive current, which means there a lot of atoms in the chamber at that stage. For loading, the drive should be less, in our case usually 140 mA is used.

6 Experimental results

After locking all our lasers to the required wavelengths, building the vacuum chamber and acquiring the needed pressure, connecting the required electronics to the trap and tuning the imaging system, we are ready to begin loading ions into the trap.

Determining the 399 wavelength, coarsely, is done by heating the oven to a pretty large temperature while applying the 399 nm laser continuously. At high enough atom density, when the laser frequency is scanned, the fluorescence from the neutral atoms is visible even with a naked eyed. An example of such neutral atom fluorescence can be seen in figure 24. This image was taken from [13] in our Sr trap, but it looks the same in the Yb trap, though no picture was taken.
This test is also done to make sure the oven is designed well enough and is capable of forming a sufficient Yb atoms flux. While loading, the flux can be significantly lowered by flowing a smaller current through the oven and heating it much less.

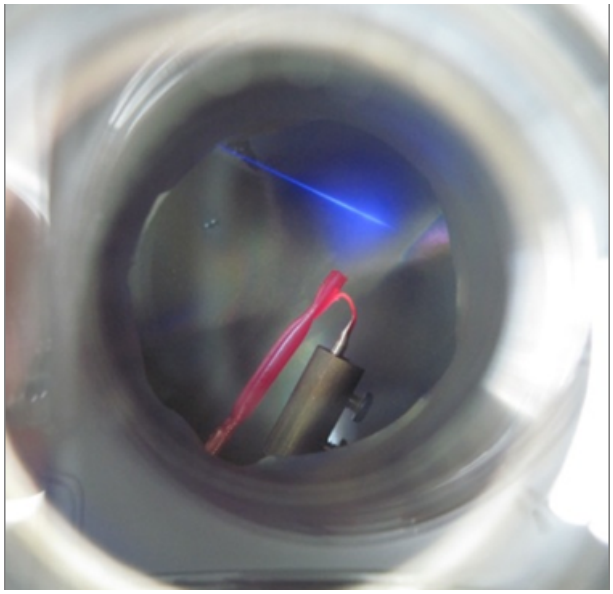

Figure 24: Picture of a Sr oven emitting high temperature neutral Sr atoms. The oven is heated by large current (thus the red color), and the atoms interact with the 422 nm laser tuned to the S-P transition. Similarly, the Yb oven was tested against the 399 nm laser.

Loading starts with heating the Yb oven, while shining all lasers into the trap center. The 369 laser should be very red detuned at this point (hundreds of MHz), since ions start very hot, and the transition is Doppler broadened. After the ion is loaded, we began seeing photons emitted from the trap center. At first, a large cloud of ions was spotted, due to a large number of ions trapped there. While imaging the cloud, we were able to better optimize the trap configurations (lasers frequency, lasers orientation, lasers focus, imaging focus, and compensation for DC electrodes).
Then, when configurations were better optimized, the same loading process was repeated, this time much slower (i.e., smaller current flowing through the oven produces a smaller rate of ionization). This resulted in the trapping of a single very well localized ion as seen in figure 25.

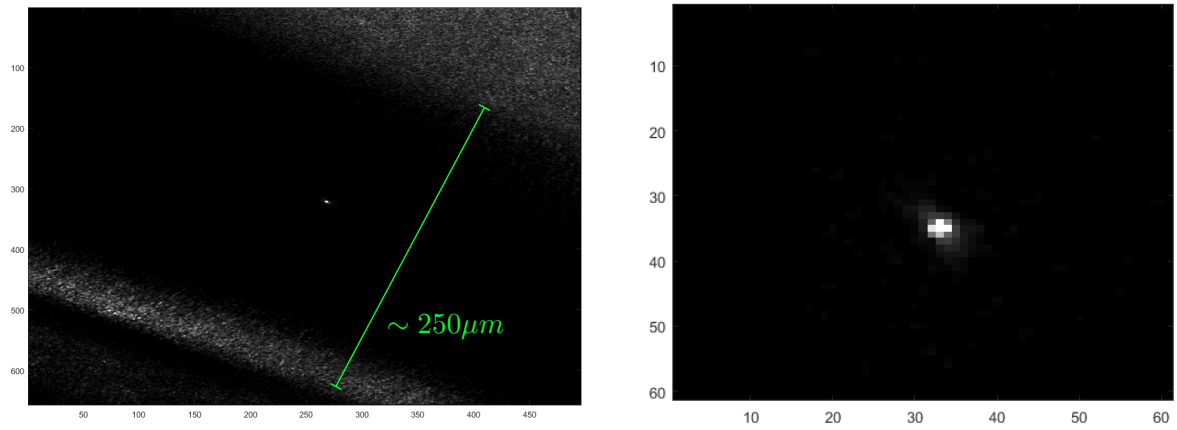

Figure 25: Single trapped $^{176}Yb^{+}$ ion. On the left a full sized image showing light reflected for the trap electrodes which are separated about $250\mu m$ from each other. On the right a zoomed in image showing only the photons emitted from the single ion.

Currently, when starting from a cold oven, loading process usually takes about a minute or two, and the ion lifetime in the trap is usually a few hours. We're currently not sure what is the limiting process for the ion lifetime in the trap, but we have some evidence of electronic noise in our trap as will be mentioned in 6.1. In the near future, we plan on better characterizing it, and trying to mitigate it and expand the ion lifetime in the trap.

6.1 Fluorescence curve

The resonance frequency of the 369.5 nm transition for $^{176}Yb^{+}$ is determined by scanning the laser frequency and measuring the resulting fluorescence. The frequency scan is performed in a random order, and between each measurement a two seconds cooling interval is performed. The fluorescence counts are recored in sixteen 100 ms intervals. The counts are averaged and background subtracted. Because of mechanical effects of the laser scattering, the ion is heated on the blue side of the resonance (i.e., in frequencies above the resonance frequency), and by that gets Doppler shifted off resonance. This effect results in a characteristic half-Lorentzian line shape [34], where the standard procedure is to identify the drop-out as resonance. The counts, plotted against the laser frequency and fitted to a Lorentzian line shape with an exponential decay are shown in figure 26.

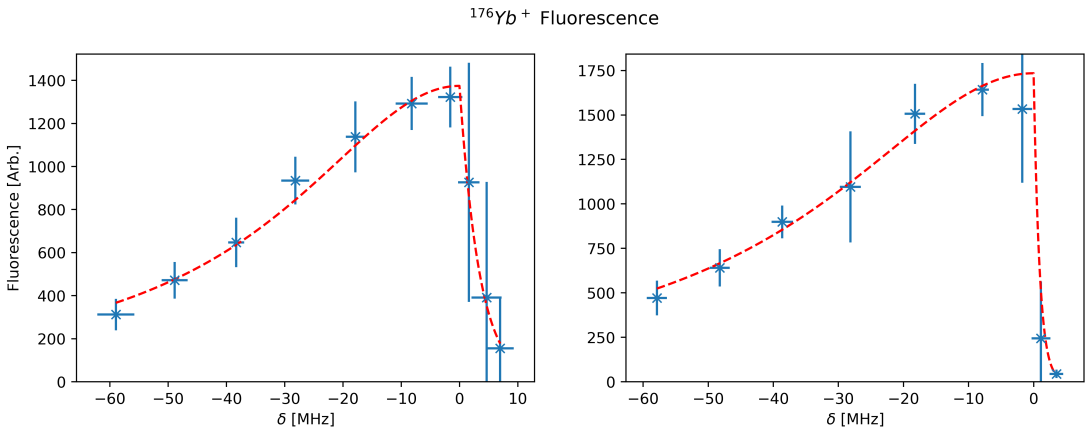

Figure 26: Fluorescence curves of a single $^{176}Yb^+$ ion for two different laser power, fitted to an half Lorentzian. This typical half-Lorentzian is obtained due to mechanical effects - blue detuned photons give energy to the ion, resulting in heating the ion and Doppler shifting it from resonance.

The data collected is fitted to the following function (half Lorentzian with exponential decay), with three free parameters:

$$\begin{aligned} F &= \frac{b}{1+\left(\frac{x-\nu_0}{d}\right)^2}\cdot H(\nu) \\ H(\nu) &= \begin{cases} 1, & \nu <= \nu_0 \\ \exp\left(-\frac{\nu-\nu_0}{e}\right), & \nu > \nu_0 \end{cases} \end{aligned} \tag{6.1}$$

From this fit the central frequency of the transition, ν_0, and the Lorentzian width, d, are extracted:

$$\begin{aligned} \nu_0 &= 811290163.1 \pm 3.2 MHz \\ d &= 35.6 \pm 1.6 MHz \end{aligned} \tag{6.2}$$

6.2 Linewidth

The Lorentzian width (d in eq. 6.2) is composed of the natural linewidth rising from spontaneous emission, but it is also power broadened according to eq. 4.24 and is given by: $d = \frac{\Gamma}{2}\sqrt{1+s_0}$. The value of s_0 parameter is hard to determine with good accuracy since the power meters in our lab are not programmed for this wavelength, and also the beam waist exactly at the trap center is hard to measure. Thus, the natural linewidth, Γ, can be evaluated by taking a few fluorescence curves as above, while scanning the intensity of the laser, and extracting it from these measurements. This was done, and the value measured is:

$$\Gamma = 18.8 \pm 9.1 MHz \tag{6.3}$$

Currently, we only done this to two different laser intensities, so the natural linewidth was extracted with very high uncertainty, In the very near future we will perform more measurements and improve on it. But still, comparing the mean value acquired with the known value of $\Gamma_0 = 19.6 MHz$ [1], we see a good fit which makes us believe this measurement makes sense.

Note: There exists another broadening to the line shape, resulting from different Zeeman levels. The laser light is applied with linear polarization, and is not perpendicular to the quantization axis. This means it have polarization components in all 3 axes (π, σ_+, σ_-), which means it can induce transitions between all Zeeman levels (i.e., $\Delta m = 0, \pm 1$ are all allowed). The transition is from the $S_{1/2}$ level to the $P_{1/2}$ level, and there is no hyperfine splitting in this isotope. Which means that at non-zero magnetic field, as we work in our lab, there is a Zeeman splitting at both levels. The resulting measured

emission spectrum is actually composed of three different transitions, with slightly different resonance frequency, one from m=-1/2 to m=1/2, the other from m=1/2 to m=-1/2 and lastly the m=±1/2 to m=±1/2. Since all these transitions occur independently, the resulting observed line profile is a convolution between all 3 Lorentzian. The Zeeman splitting from the magnetic field applied in our lab is in the order of ∼1 MHz, well below our resolving resolution. Thus, the convolution result is a slightly wider Lorentzian. To completely take this into account one needs to solve the Bloch equation for all Zeeman sub-levels as well, but since it only produces a small broadening in our case (linearly polarized laser light), this was neglected.

References

[1] Andrew D. Ludlow et al. "Optical atomic clocks". In: *Rev. Mod. Phys.* 87 (2 June 2015), pp. 637–701. DOI: 10.1103/RevModPhys.87.637. URL: https://link.aps.org/doi/10.1103/RevModPhys.87.637.

[2] L. Essen and J. V. L. Parry. "An Atomic Standard of Frequency and Time Interval: A Cæsium Resonator". In: *Nature* 176.4476 (1955), pp. 280–282. ISSN: 1476-4687. DOI: 10.1038/176280a0. URL: https://doi.org/10.1038/176280a0.

[3] W. Thomson and P. G. Tait. *Elements of Natural Philosophy*. Cambridge University Press, 1879.

[4] S. Bize et al. "Advances in atomic fountains". In: *Comptes Rendus Physique* 5.8 (2004). Fundamental metrology, pp. 829–843. ISSN: 1631-0705. DOI: https://doi.org/10.1016/j.crhy.2004.09.003. URL: http://www.sciencedirect.com/science/article/pii/S1631070504001562.

[5] M. Fischer et al. "New Limits on the Drift of Fundamental Constants from Laboratory Measurements". In: *Phys. Rev. Lett.* 92 (23 June 2004), p. 230802. DOI: 10.1103/PhysRevLett.92.230802. URL: https://link.aps.org/doi/10.1103/PhysRevLett.92.230802.

[6] S. Blatt et al. "New Limits on Coupling of Fundamental Constants to Gravity Using ^{87}Sr Optical Lattice Clocks". In: *Phys. Rev. Lett.* 100 (14 Apr. 2008), p. 140801. DOI: 10.1103/PhysRevLett.100.140801. URL: https://link.aps.org/doi/10.1103/PhysRevLett.100.140801.

[7] Cédric Delaunay et al. "Probing atomic Higgs-like forces at the precision frontier". In: *Phys. Rev. D* 96 (9 Nov. 2017), p. 093001. DOI: 10.1103/PhysRevD.96.093001. URL: https://link.aps.org/doi/10.1103/PhysRevD.96.093001.

[8] Julian C. Berengut et al. "Probing new light force-mediators by isotope shift spectroscopy". Version 1. In: (Apr. 17, 2017). arXiv: http://arxiv.org/abs/1704.05068v1 [hep-ph, physics.atm-clus, quant-ph]. URL: http://arxiv.org/abs/1704.05068v1.

[9] Wolfgang Paul. "Electromagnetic trap for charged and neutral particles". In: *Rev. Mod. Phys.* 62 (1990), pp. 531–540.

[10] N. W. McLachlan. "Mathieu Functions of Fractional Order". In: *Journal of Mathematics and Physics* 26.1-4 (1947), pp. 29–41. DOI: 10.1002/sapm194726129. eprint: https://onlinelibrary.wiley.com/doi/pdf/10.1002/sapm194726129. URL: https://onlinelibrary.wiley.com/doi/abs/10.1002/sapm194726129.

[11] D. Leibfried et al. "Quantum dynamics of single trapped ions". In: *Rev. Mod. Phys.* 75 (1 Mar. 2003), pp. 281–324. DOI: 10.1103/RevModPhys.75.281. URL: https://link.aps.org/doi/10.1103/RevModPhys.75.281.

[12] Pradip K. Ghosh. *Ion Traps*. 1st ed. International series of monographs on physics. The address: Clarendon Press, Jan. 1996. ISBN: 9780198539957.

[13] Nitzan Akerman. "Trapped ions and free photons". PhD thesis. Weizmann Institute of Science, Aug. 2018.

[14] H. P. Breuer and F. Petruccione. *The theory of open quantum systems*. Great Clarendon Street: Oxford University Press, 2002.

[15] H.J. Metcalf and Peter van der Straten. "Laser Cooling and Trapping". In: *Journal of the Optical Society of America B* 20 (May 2003). DOI: 10.1364/JOSAB.20.000887.

[16] T.W. Hänsch and A.L. Schawlow. "Cooling of gases by laser radiation". In: *Optics Communications* 13.1 (1975), pp. 68–69. ISSN: 0030-4018. DOI: https://doi.org/10.1016/0030-4018(75)90159-5. URL: http://www.sciencedirect.com/science/article/pii/0030401875901595.

[17] Dl Wineland and Hans Dehmelt. "Proposed 1014 delta upsilon less than upsilon laser fluorescence spectroscopy on t1+ mono-ion oscillator iii". In: *Bulletin of the American Physical Society*. Vol. 20. 4. AMER INST PHYSICS CIRCULATION FULFILLMENT DIV, 500 SUNNYSIDE BLVD, WOODBURY ... 1975, pp. 637–637.

[18] B. B. Blinov et al. "Quantum Computing with Trapped Ion Hyperfine Qubits". In: *Quantum Information Processing* 3.1 (Oct. 2004), pp. 45–59. ISSN: 1573-1332. DOI: 10.1007/s11128-004-9417-3. URL: https://doi.org/10.1007/s11128-004-9417-3.

[19] R. M. Godun et al. "Frequency Ratio of Two Optical Clock Transitions in $^{171}Yb^{+}$ and Constraints on the Time Variation of Fundamental Constants". In: *Phys. Rev. Lett.* 113 (21 Nov. 2014), p. 210801. DOI: 10.1103/PhysRevLett.113.210801. URL: https://link.aps.org/doi/10.1103/PhysRevLett.113.210801.

[20] C. Tamm et al. "171Yb+ Single-Ion Optical Frequency Standard at 688 THz". In: *IEEE Transactions on Instrumentation and Measurement* 56.2 (Apr. 2007), pp. 601–604. ISSN: 0018-9456. DOI: 10.1109/TIM.2007.891140.

[21] N. Huntemann et al. "Single-Ion Atomic Clock with 3×10^{-18} Systematic Uncertainty". In: *Phys. Rev. Lett.* 116 (6 Feb. 2016), p. 063001. DOI: 10.1103/PhysRevLett.116.063001. URL: https://link.aps.org/doi/10.1103/PhysRevLett.116.063001.

[22] J. E. Sansonetti and W. C. Martin. *Handbook of Basic Atomic Spectroscopic Data*. 2004. DOI: 10.1063/1.1800011. URL: https://dx.doi.org/10.18434/T4FW23.

[23] James J. McLoughlin et al. "Versatile ytterbium ion trap experiment for operation of scalable ion-trap chips with motional heating and transition-frequency measurements". In: *Phys. Rev. A* 83 (1 Jan. 2011), p. 013406. DOI: 10.1103/PhysRevA.83.013406. URL: https://link.aps.org/doi/10.1103/PhysRevA.83.013406.

[24] John Bechhoefer. "Feedback for physicists: A tutorial essay on control". In: *Rev. Mod. Phys.* 77 (3 Aug. 2005), pp. 783–836. DOI: 10.1103/RevModPhys.77.783. URL: https://link.aps.org/doi/10.1103/RevModPhys.77.783.

[25] J. D. Siverns et al. "On the application of radio frequency voltages to ion traps via helical resonators". In: *Applied Physics B* 107.4 (June 2012), pp. 921–934. ISSN: 1432-0649. DOI: 10.1007/s00340-011-4837-0. URL: https://doi.org/10.1007/s00340-011-4837-0.

[26] Carl E. Wieman and Leo Hollberg. "Using diode lasers for atomic physics". In: *Review of Scientific Instruments* 62.1 (1991), pp. 1–20. DOI: 10.1063/1.1142305. eprint: https://doi.org/10.1063/1.1142305. URL: https://doi.org/10.1063/1.1142305.

[27] A. S. Arnold, J. S. Wilson, and M. G. Boshier. "A simple extended-cavity diode laser". In: *Review of Scientific Instruments* 69.3 (1998), pp. 1236–1239. DOI: 10.1063/1.1148756. eprint: https://doi.org/10.1063/1.1148756. URL: https://doi.org/10.1063/1.1148756.

[28] O. I. Permyakova, A. V. Yakovlev, and P. L. Chapovsky. *Simple external cavity diode laser*. 2003. eprint: arXiv:physics/0312047.

[29] Christopher J Erickson et al. "An Ultra-High Stability, Low-Noise Laser Current Driver with Digital Control". In: *The Review of scientific instruments* 79 (Aug. 2008), p. 073107. DOI: 10.1063/1.2953597.

[30] Daylin L Troxel, Christopher J Erickson, and Dallin Durfee. "Note: Updates to an ultra-low noise laser current driver". In: *The Review of scientific instruments* 82 (Sept. 2011), p. 096101. DOI: 10.1063/1.3630950.

[31] T.A Heumier and J.L. Carlsten. *Mode Hopping in Semiconductor Lasers*. URL: https://www.newport.com/medias/sys_master/images/images/h4b/h48/8797049585694/AN08-Mode-Hopping-in-Semiconductor-Laser-Diodes.pdf.

[32] Richard W. Fox, Chris W. Oates, and Leo W. Hollberg. "1. Stabilizing diode lasers to high-finesse cavities". In: Experimental Methods in the Physical Sciences 40 (2003). Ed. by Roger D. van Zee and J. Patrick Looney, pp. 1–46. ISSN: 1079-4042. DOI: https://doi.org/10.1016/S1079-4042(03)80017-6. URL: http://www.sciencedirect.com/science/article/pii/S1079404203800176.

[33] Alexander Franzen. *ComponentLibrary*. http://www.gwoptics.org/ComponentLibrary/.

[34] Sara Ejtemaee. "A fluorescence study of single trapped ytterbium ions for quantum information applications". PhD thesis. Simon Fraser University, 2010.